The Limits of The Quasi-Harmonic Approximation: Anharmonicity in Germanium and the Entropy of Melting

Shiva Mudide

In Partial Fulfillment of the Requirements for the
Degree of
Bachelor of Science in Physics

Adviser: Prof. Brent Fultz and Camille Bernal

California Institute of Technology

June 2021

Abstract

Inelastic Neutron Scattering (INS) measurements were made at the Wide Angular-Range Chopper Spectrometer (ARCS) on Germanium at temperatures higher than what has been done before, from 296 K to 1203 K. Raw data was used to calculate the dynamic structure factor. Multi-phonon and multiple scattering events were accounted for and subtracted. These dynamic structure factors were then used to calculate single phonon density of states (DOS) for temperatures throughout the said temperature range. Thermal softening of the phonon modes was observed. The softening was quantitatively characterized with several gruneisen parameters to better understand the effects phonon anharmonicity in Germanium. We find the quasiharmonic approximation alone cannot explain the large phonon softening. The vibrational entropy contribution to the total entropy was also determined. We find that the vibrational entropy makes up almost all of the total entropy in Germanium, even at elevated temperatures.

We also conduct melting experiments to ensure containment of Si, Bi, and Pb in quartz ampules. These metals will be heated through their melting points at ARCS in the near future in order to determine the vibrational entropy contribution to the latent heat of melting. Furthermore, we write an algorithm based on the work of Sivia to determine the number of phonon modes there is the maximum evidence for in any given phonon DOS.

Contents

Listing of figures

For my little brother, Anish.

Acknowledgments

I WOULD FIRST LIKE TO THANK my thesis advisor, Prof. Fultz. I am extremely grateful that he took me on into his lab last year. For me, this thesis and the work I have done under his guidance has been transformative in not only my career path for at least the next few years, but also in my sense of purpose. I have found something that I genuinely enjoy, something that I am excited to think about on a daily basis. There is nothing more that I want to do over the next few years than continue to pursue more research. This joy only grew as I learned more and more about the material surrounding my thesis. I am indebted to Prof. Fultz for giving me the opportunity to feel this way so early in my career.

I would also like to deeply thank my graduate student advisor, Camille. I mean it when I say that this thesis would not have happened without her guidance. Camille allowed me the independence to learn and grow as a researcher on my own. She is busy with her own PhD but is somehow always able to find the time to collaborate with me when I reach out. She is incredibly intelligent and knowledgeable about phonons and INS. I don't think I've ever asked her a question that she couldn't come up with an answer to (besides where does the entropy of melting come from!). I have learned so much from Camille and I hope to continue collaborating in the future.

Camille, along with everyone in the Fultz lab, is remarkably kind and genuine. They immediately took me in and helped me get started in the lab. They have continued to be a huge support throughout the entire year. Thank you, all.

I am afraid neutrons will not be of any use to any one.

Sir James Chadwick

1

Inelastic Neutron Scattering

Neutrons can be scattered by both the unpaired electrons of magnetic atoms and the nuclei of those atoms themselves. The former is referred to as magnetic scattering while the latter is nuclear scattering. When experiments occur at neutron scattering facilities like the Wide Angular-Range Chopper Spectrometer (ARCS), the essential idea is that a monochro-

matic beam of neutrons is scattered off a sample. The raw data is in the form of the flux of neutrons scattered as a function of the momentum and energy transfer [3].

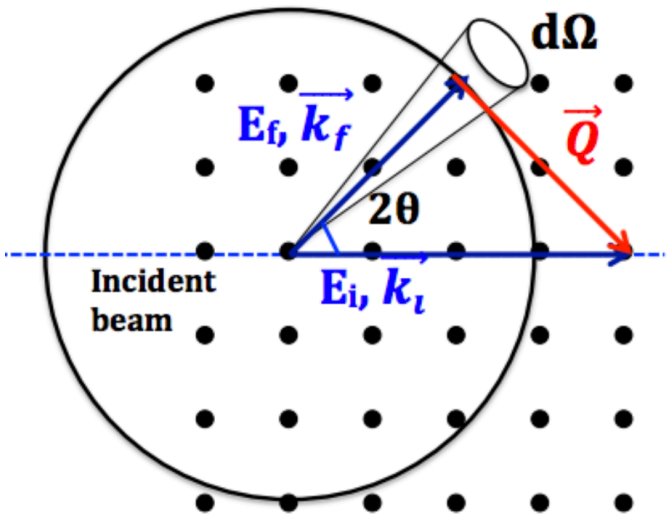

Figure 1.1: Incident Neutrons Scattered into Final State

In figure 1.1 we have let the incident beam be defined by its de Broglie wavevector $\vec{k_i}$ and energy $\vec{E_i}$. Because we generally have a lossless isotropic medium, like any cubic crystal, the direction of the wavevector is the same as the direction of wave propagation. The scattered wave is defined by $\vec{k_f}$ and $\vec{E_f}$.

From conservation of momentum and energy we can obtain,

$$\vec{Q} = \vec{k_i} - \vec{k_f} \tag{1.1}$$

$$\hbar\omega = E_i - E_f \tag{1.2}$$

We refer to $\vec{Q}$ as the momentum transfer. We generally distinguish between two (and sometimes three) different types of scattering. The first is elastic scattering. This is when there is indeed momentum transfer, so $\vec{Q}$ is nonzero, but the magnitude of $\vec{k_f}$ and $\vec{k_i}$ are the same.

Neutrons behave as matter waves, so we can express their energy in terms of their frequency and their momentum in terms of their wavenumber by the de Broglie relations,

$$E = \hbar\omega, p = \hbar k \tag{1.3}$$

This yields a dispersion relation for neutrons, which in the non-relativistic limit is $E = \frac{\hbar^2 k^2}{2m}$.

We can then write the energy conservation as,

$$\Delta E = \hbar\omega = \frac{\hbar^2}{2m}(k_i^2 - k_f^2) \tag{1.4}$$

We therefore see that for elastic scattering, when the magnitude of $\vec{k_i}$ equals that of $\vec{k_i}$, the energy transfer is zero.

The second type of scattering is inelastic scattering, when the magnitude of $\vec{k_i}$ does not equal that of $\vec{k_f}$ due to some energy gain or loss when the neutrons are scattered by the sample. We think of the change in energy as due to the creation or destruction of excitations in the sample, which can be used to gain information about the underlying dynamics within a material [3].

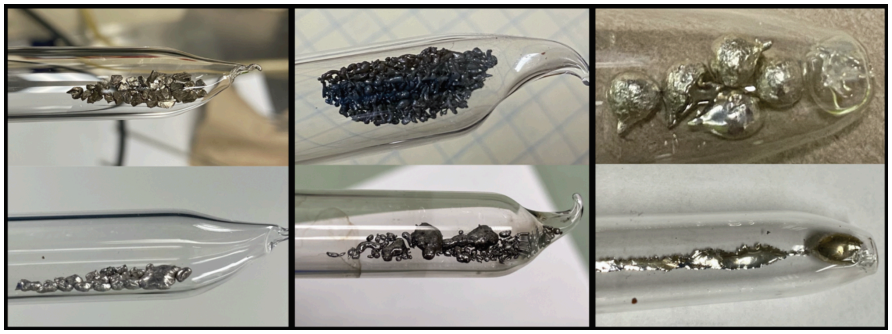

Figure 1.2: Bi, Pb, and Sn sealed in evacuated quartz ampules before (top) and after (bottom) melting in preparation for neutron scattering at ARCS. In this thesis we will primarily be analyzing neutron scattering done on Ge in a similar ampule.

1.1 Significance of $S(\vec{Q}, \omega)$

Exactly how the various changes in energy can be related the underlying dynamics is often situational and complex, but the basic idea will still be explained.

The flux of neutrons scattered as a function of the momentum and energy transfer is referred to as $S(\vec{Q}, \omega)$. Neutron scattering directly measures $S(\vec{Q}, \omega)$. $S(\vec{Q}, \omega)$ can be related to the double differential cross section by the methods of Van Hove [4],

$$\frac{d^2\sigma}{d\Omega dE} = N\frac{k_f}{k_i}S(\vec{Q}, \omega) \tag{1.5}$$

The double differential cross section is the number of neutrons scattered into solid angle $d\Omega$ per second with energy between E and $E + dE$. This is, of course, normalized by the incident flux. For magnetic scattering, the potential is not short range but it is weak. We see the opposite in nuclear scattering, in which the potential is short range but it is strong. We can use Fermi's golden rule for first order perturbation theory to find the probability of

transitions. The scattering process is then the same as the Born approximation [3].

For a change in wavevector from $\vec{k_i}$ to $\vec{k_f}$, the double differential cross section is then,

$$\frac{d^2\sigma}{d\Omega dE_{\vec{k_i}\to\vec{k_f}}} = N\frac{k_f}{k_i}\left(\frac{m}{2\pi\hbar^2}\right)^2 |\left\langle k_f\sigma_f\lambda_f\right| V\left|k_i\sigma_i\lambda_i\right\rangle|\delta(E_{\lambda i} - E_{\lambda f} + E_i - E_f) \tag{1.6}$$

Where λ_i and λ_f are the initial and final states of the sample, respectively. σ is the scattering cross section for the neutron beam. In the Born approximation the potential interaction matrix elements from equation 1.6 can be calculated.

We could also relate the double differential cross section to the Van Hove function, a time dependent pair correlation function. This gives us the correlations between the position of one nucleus at time $t = 0$ with another nucleus as time t, measuring the strength of correlations within our material. As well will see soon, $S(\vec{Q}, \omega)$ encapsulates much of the underlying dynamics within our material.

The career of a young theoretical physicist consists of treating the harmonic oscillator in ever-increasing levels of abstraction.

Sydney Coleman

2

Phonons and Anharmonicity

2.1 Crystal Lattice

A LATTICE GRAPH IS A GRAPH whose drawing, embedded in some Euclidean space $\mathbb{R}^n$, forms a regular tiling. It turns out that this mathematical concept of a graph can also be

used to accurately describe physical crystalline solids at low temperature. The fundamental concept we use is the Bravais lattice, which describes the long-range regular tiling of physical crystals. It allows us to reduce the arrangements of atoms in the crystal to a set of translation symmetry operations.

We define a unit cell by integer linear combinations of three independent vectors $\mathbf{a}_1$, $\mathbf{a}_2$, and $\mathbf{a}_3$, the primitive lattice vectors in the crystal. We repeat this unit cell to generate the entire crystal lattice. We define the unit cell as the smallest cell that can generate the entire crystal. Labeling each unit cell by a triplet of integers $l = (l_1, l_2, l_3)$, yields:

$$\mathbf{R}_l = l_1\mathbf{a}_1 + l_2\mathbf{a}_2 + l_3\mathbf{a}_3 \tag{2.1}$$

for the equilibrium position of the origin of the lth unit cell ($\mathbf{R}_l = \mathbf{x}_l$).

We can go two steps further and describe not only the equilibrium position of any atom in any cell, but also the time-dependent position of any such atom. We may define the equilibrium positions with respect to the origin of a unit cell for each atom, κ, by the vector $\mathbf{x}_\kappa$ for $\kappa = 1, 2, , N$.

The equilibrium position of atom κ in cell l is then:

$$\mathbf{x}_{l\kappa} = \mathbf{x}_l + \mathbf{x}_\kappa. \tag{2.2}$$

We may also consider the displacement of the κth atom from its equilibrium, $\mathbf{u}_\kappa$, and therefore define the instantaneous position as

$$\mathbf{r}_{l\kappa}(t) = \mathbf{x}_{l\kappa} + \mathbf{u}_{l\kappa}(t) \tag{2.3}$$

There are actually only 5 Bravais lattices in 2 dimensions and 14 in 3 dimensions (figure 2.1).

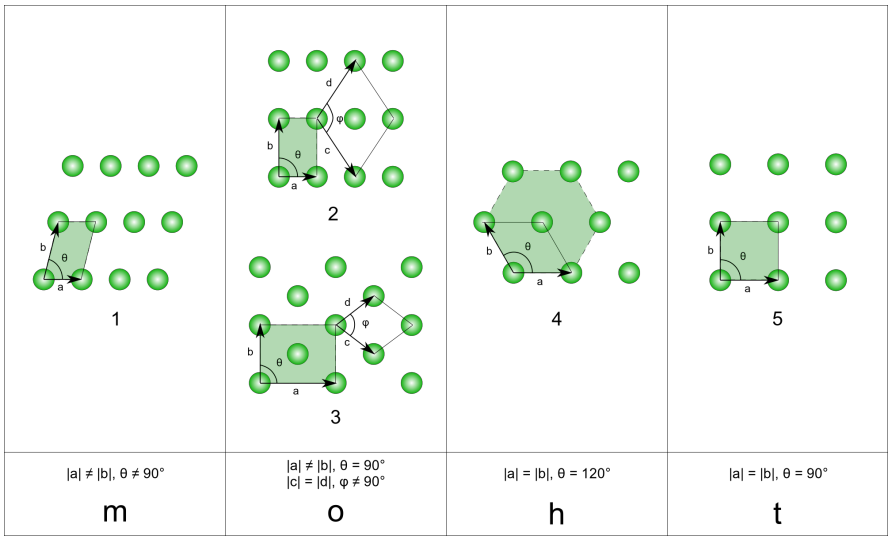

Figure 2.1: All 5 two-dimensional Bravais lattices [1]

It is often convenient, and preferred, to convert a Bravais lattice to reciprocal space. Since there exists a set of plane waves with the same periodicity as the original lattice, we may Fourier transform the real space domain to its momentum k-space.

$$\exp(i\mathbf{K} \cdot \mathbf{R}_l) = 1. \tag{2.4}$$

The reciprocal lattice, $\mathbf{K}$, is then generated by

$$\mathbf{q} = y_1\mathbf{b}_1 + y_2\mathbf{b}_2 + y_3\mathbf{b}_3, \tag{2.5}$$

similar to how $\mathbf{R}_l$ was generated by eq.2.1.

The prefactors y_i are again integers and $\mathbf{b}_1$, $\mathbf{b}_2$, $\mathbf{b}_3$ are defined as the primitive vectors of the

reciprocal lattice.

We can convert between the reciprocal space vectors and the real space vectors by

$$\mathbf{b}_1 = 2\pi \frac{\mathbf{a}_2 \times \mathbf{a}_3}{\mathbf{a}_1 \cdot \mathbf{a}_2 \times \mathbf{a}_3}, \mathbf{b}_2 = 2\pi \frac{\mathbf{a}_3 \times \mathbf{a}_1}{\mathbf{a}_1 \cdot \mathbf{a}_2 \times \mathbf{a}_3}, \mathbf{b}_3 = 2\pi \frac{\mathbf{a}_1 \times \mathbf{a}_2}{\mathbf{a}_1 \cdot \mathbf{a}_2 \times \mathbf{a}_3} \tag{2.6}$$

The primitive cell of reciprocal space is commonly referred to as the first Brillouin zone.

2.2 Phonons

With the crystal lattice structure described above in mind, we can imagine these (classical) atoms sitting at their equilibrium positions at 0 K. As temperature increases, the atoms begin to vibrate, oscillating about their equilibrium positions.

Quantum mechanics tells us that there is actually a zero point energy, so the atoms are already in motion even at 0 K. Quantum mechanics (initially Einstein, actually) further tells us that these vibrations are discretized and can be thought of as individual packets of energy that have frequencies that are dependent on the specific material at hand. These discrete vibrations are phonons.

For a basic model we may consider a system of n point-masses connected by harmonic springs. This yields 3 translational degrees of freedom and $3n - 3$ vibrational degrees of freedom, for a total of $3n$ equations of motion. This is solvable, but quite difficult to do so when n becomes large.

These equations of motion will be coupled. We may introduce a change of variables to decouple the system so that it becomes what is not really a system at all. By decoupling we can solve separately for each variable, instead of being forced to solve for them all together

at the same time. This is commonly done by diagonalizing the dynamical matrix from the original, coupled equations of motion.

The advantage here is not just in the ease of solution. There must also be something physical going on, some physical insight behind these new variables.

Solving the uncoupled equations yields $3n-3$ normal modes for most geometrical arrangements. These modes are "normal" because they are all independent of each other. Physically, there is no energy transfer between the normal harmonic modes.

The same idea is applied more rigorously to periodic lattices in the next section. Indeed, in periodic lattices the evenly spaced energy levels of these normal modes are how phonons are defined more precisely.

2.3 Harmonic approximation

In what we refer to as the "harmonic approximation" the bonds between atoms are treated as Hooke's law obeying springs, and the potentials are therefore a quadratic function of atom displacements. Not all the properties of the lattice are accurately described by the harmonic approximation, but it at least accurately predicts the number of phonons we observe in a material.

We treat the lightweight electrons as the interatomic "glue" between atoms. We use the Born-Oppenheimer approximation, and assuming the nuclei respond instantly to displacements, consider only nuclear motions. The Hamiltonian is then,

$$H_n = \sum_{l,\kappa} \frac{\rho_{l\kappa}^2}{2m_\kappa} + \phi. \tag{2.7}$$

The potential energy, ϕ, is the sum of the contribution from every pair of atoms in the crystal. We can expand the potential energy in terms of powers of the atomic displacements from their equilibrium positions using a multivariate taylor series as,

$$\phi = \phi_0 + \sum_{\alpha l \kappa} \phi_{\alpha l \kappa} u_{\alpha l \kappa} + \frac{1}{2} \sum_{\alpha l \kappa} \sum_{\alpha' l' \kappa'} \phi_{\alpha \alpha' l \kappa l' \kappa'} u_{\alpha l \kappa} u_{\alpha' l' \kappa'} + \ldots, \tag{2.8}$$

where $\alpha = \{x, y, z\}$ are the Cartesian components and the coefficients of the Taylor series are the derivatives of the potential with respect to the displacements

$$\phi_{\alpha l \kappa} = \left. \frac{\partial \phi}{\partial u_{\alpha l \kappa}} \right|_0, \tag{2.9}$$

$$\phi_{\alpha \alpha' l \kappa l' \kappa'} = \left. \frac{\partial^2 \phi}{\partial u_{\alpha l \kappa} \partial u_{\alpha' l' \kappa'}} \right|_0. \tag{2.10}$$

The first partials, of course, vanish at equilibrium, so

$$\phi_{\alpha l \kappa} = 0 \tag{2.11}$$

In the harmonic approximation we ignore terms higher than order two in the displacements.

We can rewrite the 2nd partial in matrix form for each pair of atoms $l\kappa, l'\kappa'$ where $(l, \kappa) \neq (l_0, \kappa_0)$ as,

$$\phi_{l\kappa, l'\kappa'} = \begin{bmatrix} \varphi_{xx} & \varphi_{xy} & \varphi_{zz} \\ \varphi_{yx} & \varphi_{yy} & \varphi_{yz} \\ \varphi_{zx} & \varphi_{zy} & \varphi_{zz} \end{bmatrix}. \tag{2.12}$$

This yields a hamiltonian in matrix form:

$$H_n = \sum_{l\kappa} \frac{\rho_{l\kappa}^2}{2m_\kappa} + \phi_0 + \frac{1}{2} \sum_{l\kappa} \sum_{l'\kappa'} \mathbf{u}_{l\kappa}^T \phi_{l\kappa l'\kappa'} \mathbf{u}_{l'\kappa'}. \tag{2.13}$$

κ and κ_0 act as specific types of atoms. The relative nearest neighbor distance between cells l and l_0 is used to specify their distance.

By Newton's third law, the matrix must be real and symmetric. This means the diagonalization of the matrix can be done merely by transforming to the eigenbasis, where the eigenvectors are real and orthonormal.

By Newton's second law, the equations of motion for the nuclei are,

$$M_\kappa \ddot{\mathbf{u}}_{l\kappa} = -\sum_{l'\kappa'} \phi_{l\kappa,l'\kappa'} \mathbf{u}_{l',\kappa'} \tag{2.14}$$

Assuming periodic boundary conditions yields plane wave solutions for the displacements:

$$\mathbf{u}_{l\kappa} = \frac{1}{\sqrt{M_\kappa}} \mathbf{e}_{j\kappa}(\mathbf{q}) \exp\big(i[\mathbf{q} \cdot \mathbf{x}_l - \omega_j(\mathbf{q})t]\big) \tag{2.15}$$

Taking the real part gives physical displacements.

$\mathbf{q}$ is the wave vector, $\omega_j(\mathbf{q})$ is the angular frequency, $\mathbf{e}_{j\kappa}(\mathbf{q})$ is the polarization, and j is the branch index.

We could substitute the propagating wave displacements into the equations of motion, or alternatively, we could note that this is the same as taking the space Fourier transform of the right hand side.

We are then reduced to solving,

$$\omega_j^2(\mathbf{q})\mathbf{e}_{j\kappa}(\mathbf{q}) = \sum_{\kappa'} \mathbf{D}_{\kappa\kappa'}(\mathbf{q})\mathbf{e}_{j\kappa'}(\mathbf{q}). \tag{2.16}$$

This is called the dynamical matrix expression, where $\mathbf{D}(\mathbf{q})$ is the dynamical matrix [5]. Every pair of atoms in the crystal has a force constant associated with it. This matrix contains the force contents for all pairs. To aid in computation we may truncate the matrix to include only nearest-neighbor restoring forces. This usually does not result in a significant loss of accuracy because the largest contribution to any given restoring force for an atom comes from its immediately adjacent partners.

For every $\mathbf{q}$ in reciprocal space, we may solve for the normal mode frequencies ω and associated mode wavevectors. In this sense we generate the normal mode frequencies and wavevectors as a function of $\mathbf{q}$.

We now must simply diagonalize $\mathbf{D}(\mathbf{q})$ at a large number of $\mathbf{q}$ to find the decoupled modes. $\hbar\omega_j(\mathbf{q})$ is the energy of the state associated with $\mathbf{e}_j(\mathbf{q})$.

Thankfully, $\mathbf{D}(\mathbf{q})$ is Hermitian for any value of $\mathbf{q}$, so its eigenvectors can be made to be orthonormal with real eigenvectors. The diagonalization also only involves the use of one orthogonal matrix.

2.4 Thermodynamics

In the dynamical matrix methodology, we are able to connect the symmetry of the lattice with the interatomic forces driving the allowed normal modes. Let's try to calculate some basic thermodynamic properties under the previous assumptions.

In our expansion of the potential, U_0 is the binding energy of the system, and the next term describes a classical three-dimensional simple harmonic oscillator (SHO). The partition function for the crystal with N atoms, and therefore, $3N$ oscillators is,

$$Z_N^{\text{SHO}} = A^N (k_B T)^{3N} \exp\left(-\frac{NU_0}{k_B T}\right) \tag{2.17}$$

where A is constant, T is the temperature, and k_B is the Boltzmann constant. The free energy is $F = E + PV - TS = E + PV - k_B T \ln(Z)$, where E is the energy, P is the pressure, V is the volume, and S is the entropy. Differentiating F with respect to T yields the entropy. The heat capacity at constant volume is then,

$$C_V^{\text{SHO}} = T\frac{\partial S}{\partial T}\Big|_V = 3Nk_B. \tag{2.18}$$

This is known as the Dulong and Petit limit. It accurately describes the heat capacity of many solids at temperatures higher than room temperature. Without quantization, however, we are unable to capture the fact that the heat capacities of solids actually goes to zero as temperature goes to zero.

Extending this description of lattice modes to quantized vibrational excitations allows us to capture the vanishing nature of the heat capacity (Debye went a step further and was able to capture the T^3 power law that the heat capacity decays at by assuming that the frequencies in a material can vary as a function of the wavevector).

The quantum representation of the hamiltonian is,

$$H = \sum_{\mathbf{k},s} \hbar\omega_s(\mathbf{k})(\alpha_{\mathbf{k}s}^\dagger \alpha_{\mathbf{k}s} + \frac{1}{2}) = \sum_{\mathbf{k},s} (n_{\mathbf{k}s} + \frac{1}{2})\hbar\omega_s(\mathbf{k}), \tag{2.19}$$

where the phonon creation operator $\alpha^{\dagger}_{\mathbf{k}s}$ and phonon annihilation operator $\alpha_{\mathbf{k}s}$ are defined as

$$\alpha^{\dagger}_{\mathbf{k}s} = \frac{1}{\sqrt{N}} \sum_i e^{-i\mathbf{k}\cdot r_i} \varepsilon_s(\mathbf{k}) \left[\sqrt{\frac{M\omega_s(\mathbf{k})}{2\hbar}} \mathbf{u}_i - i \sqrt{\frac{1}{2\hbar M\omega_s(\mathbf{k})}} \rho_i \right] \tag{2.20}$$

and

$$\alpha_{\mathbf{k}s} = \frac{1}{\sqrt{N}} \sum_i e^{-i\mathbf{k}\cdot r_i} \varepsilon_s(\mathbf{k}) \left[\sqrt{\frac{M\omega_s(\mathbf{k})}{2\hbar}} \mathbf{u}_i + i \sqrt{\frac{1}{2\hbar M\omega_s(\mathbf{k})}} \rho_i \right] \tag{2.21}$$

and

$$n_{ks} = (e^{\frac{\hbar\omega_s(k)}{k_B T}} - 1)^{-1}. \tag{2.22}$$

Based on the above analysis it is clear that, in the harmonic approximation, we assume that phonon spectra, like their dispersion relations or density of states, remain constant as a function of temperature [6]. We would therefore calculate the phonon contributions to properties of a material at a single temperature and assume that those contributions apply at all other temperatures. This notion is clearly not true in real materials.

We can now again calculate some thermodynamic properties, assuming our new quantum mechanical framework.

From the hamiltonian the possible energies of a quantum harmonic oscillator with frequency ω are $E_n = (n + \frac{1}{2})\hbar\omega$.

To find the partition function for a single oscillator with frequency ω_i, we sum over all energies and substitute the summation by a geometric series to yield,

$$Z_1^{\mathrm{QHO}} = \frac{\exp(-\hbar\omega_i\beta/2)}{1 - \exp(-\hbar\omega_i\beta)}. \tag{2.23}$$

We have let $\beta = 1/(k_B T)$.

The partition function for N atoms and $3N$ independent oscillators is then,

$$Z_N^{\text{QHO}} = \prod_i^{3N} \frac{\exp(-\hbar\omega_i\beta/2)}{1-\exp(-\hbar\omega_i\beta)}. \tag{2.24}$$

We remember not to divide by $N!$ because the sites are distinguishable.

From the partition function we can recover all desirable thermodynamic functions. The entropy from phonon vibrations is,

$$S_{\text{vib}} = k_{\text{B}} \sum_i^{3N} \left[-\ln\left(1 - \frac{1}{\exp(\hbar\omega_i\beta)}\right) + \frac{\hbar\omega_i\beta}{\exp(\hbar\omega_i\beta)-1} \right]. \tag{2.25}$$

In the Einstein model, $\omega_i = \omega_E$ for all i, so the heat capacity is given by

$$C_V^{\text{Ein}} = 3Nk_{\text{B}}(\hbar\omega_E\beta)^2 \frac{\exp(\hbar\omega_E\beta)}{[\exp(\hbar\omega_E\beta)-1]^2}. \tag{2.26}$$

We can easily determine the limiting cases of the heat capacity.

When $T \to \infty$, L'Hopital's rule shows that the heat capacity goes to $3Nk_{\text{B}}$, which recovers the Dulong and Petit limit as before.

When $T \to 0$, the heat capacity also goes to zero, matching experimental evidence.

Furthermore, phonons are bosons, so they follow Bose-Einstein statistics. Their chemical potential is zero and their occupation can be described by the Planck distribution, because they are not conserved.

The Planck distribution is

$$\mathrm{n}_T(E) = \frac{1}{\exp(E\beta)-1}. \tag{2.27}$$

Inserting this into our expression for S_{vib} reduces it to

$$S_{\text{vib}} = Nk_{\text{B}}[(1 + \text{n}_T)\ln(\text{n}_T) - \text{n}_T\ln(\text{n}_T)]. \tag{2.28}$$

We often, however, work with a phonon density of states (DOS), $g(E)$. This is a distribution of the different phonon modes with respect to energy.

If we assume the energies follow such a distribution, $g(E)$, which is normalized to unity, we can write S_{vib} as,

$$S_{\text{vib}}(T) = 3k_{\text{B}}\int_0^\infty g(E)[(1 + \text{n}_T(E))\ln(\text{n}_T(E)) - \text{n}_T(E)\ln(\text{n}_T(E))]\,\mathrm{d}E. \tag{2.29}$$

Note that the only temperature dependence here comes from the Planck distribution. The phonon DOS curves can be measured in a few ways. The most apparent is by calculated phonon dispersions assuming certain approximations like the Einstein or Debye approximation. We could also use experimental phonon dispersions or even inelastic neutron scattering (INS). Phonon DOS curves obtained through INS play a central role in this thesis. Furthermore, the harmonic approximation correctly predicts that the phonon free energy will change as a function of temperature. Since $F_{\text{vib}} = -TS_{\text{vib}}$, the magnitude of the phonon free energy increases as T increases.

Additionally, as we have shown before, the phonon entropy itself, S_{vib}, also increases with temperature from its dependence on the Planck distribution.

The phonon free energy can therefore be thought of as the sum total of the energies of all the phonons populated in a material. The phonon DOS contributes the amount of available phonon modes available in the material. F_{vib} accounts for both this availability and the

likelihood that there is enough energy in the system to populate any of these modes. So even though the harmonic approximation products that phonon DOS will remain fixed with temperature, which we know is not the case, it still allows for higher energy phonon modes to be populated more frequently at higher temperatures. This is how it is still able to correctly predict the magnitude of phonon entropy even at elevated temperatures. In fact, the phonon entropy in the harmonic approximation actually turns out to be quite accurate even when we consider higher order terms in the potential between atoms, especially when we substitute the DOS for the correct experimental DOS at any given temperature.

2.5 Failures of the Harmonic Approximation

So the harmonic approximation gets us quite far, but it clearly has its shortcomings. The most obvious one is thermal expansion. The harmonic approximation assumes fixed, temperature-independent volumes, with fixed spring constants. Interestingly, even if we did not know about thermal expansion from experiment, we could remember that the equilibrium volume of a material is the volume that minimizes its free energy. But even given a fixed, harmonic phonon DOS, the phonon free energy increases with temperature! We therefore expect temperature dependent equilibrium volumes of materials from minimizing this temperature dependent free energy.

There are other anhominicites that usually become apparent at higher temperatures. This is because even though the potential between atoms could be almost arbitrary, we can approximate it, as we have done, by a quadratic potential about its minimum. The harmonic approximation therefore often works better at lower temperatures, where the atomic displacements

are small and the quadratic potential is more accurate. The harmonic approximation assumes that phonon modes are independent and non-interacting. This is not true in a real material, as there can also be interactions between phonons at all temperatures, but this is more common at higher temperatures, because more phonons populate the material, so the probability that any given phonon encounters another one is larger.

2.6 Quasi-harmonic Approximation

The quasi-harmonic approximation attempts to rectify some of the shortcomings of the harmonic approximation. It maintains the notion of harmonic, non-interacting phonons, while accommodating for fact that materials have temperature-induced volume changes. While the harmonic approximation predicts static phonon spectra, the changing volumes in the QHA elicit varying phonon spectra.

It is important to note though, that the temperature induced volume changes are the only reason the phonon spectra are expected to vary as a function of temperature. All the effects of temperature on the phonon DOS and dispersions are from thermal expansion, so even the QHA does not take into account interacting phonon modes.

Still, the QHA does predict some interesting features of materials.

The intuition for the QHA can come from our original quadratic, ball and spring model of the crystal in the harmonic approximation. If we let the spring constants between atoms decrease and become "softened," the equilibrium positions of the balls would become further apart. Fixed atom displacements (from the harmonic approximation to the QHA) would result in a lower potential energy stored in the springs.

Extending this intuition to the phonon DOS, we would expect that phonon frequencies would decrease with increasing volume. We refer to this decrease in the phonon frequencies as phonon "softening."

In a typical material we therefore expect that rising temperatures lead to thermal expansion and a softening of phonon frequencies. When the temperature is reduced we expect thermal contraction and increasing phonon frequencies.

To underscore, the QHA differs from the harmonic approximation in that although we still assume a harmonic potential at each temperature, this potential varies as a function of temperature, which elicits the shifting phonon DOS.

Furthermore, the QHA also avoids the nonsensical vanishing equilibrium pressure and bulk modulus that the harmonic approximation predicts.

Remember that if the free energy does not depend on V, P and B vanish because

$$P = -\left(\frac{\partial F}{\partial V}\right)\Big|_{T,N} \tag{2.30}$$

and

$$B = -V\frac{\partial P}{\partial V}\Big|_{T,N}. \tag{2.31}$$

A nice way of quantifying the frequency shifts for different materials is the Gruneisen parameter.

The change in frequency of all the phonons is proportional to the change in volume with increasing temperature, so

$$\frac{\Delta\omega}{\omega} = -\gamma\frac{\Delta V}{V}, \tag{2.32}$$

where γ is known as the Gruneisen parameter. For most materials, its value is around 1-2. A

larger Gruneisen parameter means that the phonon modes see greater shifts in frequency for a given thermal expansion.

We could also consider the changes in frequency for the individual phonon modes. This results in a similar definition for the mode Gruneisen parameter γ_i.

The QHA is therefore very similar to the harmonic approximation, just that the spring constants between the atoms vary as a function of temperature, leading to shifting frequencies. We can therefore use the same expression for the vibrational entropy as before. Alternatively, we could separate out the entropy of dilation from the entropy at zero thermal expansion. The entropy of dilation can be found by integrating the difference between the heat capacity at constant pressure and volume. Namely,

$$S_{\mathrm{ph,D}} = S_{\mathrm{ph,D}}(T) = \int_0^T \frac{C_P - C_V}{T'}\,\mathrm{d}T' = \int_0^T \frac{9K_T\alpha^2}{\rho_N}\,\mathrm{d}T', \tag{2.33}$$

where T is the temperature, K_T is the isothermal bulk modulus, α is the linear coefficient of thermal expansion, and ρ_N is the number density. We expect these two methods of accounting for the entropy to yield the same answer, but this is not always true. We refer to any entropy not accounted for by the quasiharmonic model as anharmonic phonon entropy.

2.7 Anharmonicity

The QHA is still a relatively simple model and it has its own flaws, so it does not predict all the observations we see in experiments. We refer to any effects not predicted by the QHA as anharmonic effects.

The most conspicuous flaw is that QHA assumes that phonons are entirely independent

normal modes with infinite lifetimes. This leads to predictions of infinite thermal conductivity, and that measured phonon peaks should have no linewidths (other than those that are generated by the instrument resolution function).

In real materials we know that phonons do indeed interact with each other and with other collective excitations.

Phonon scattering events indicate that true phonons have finite lifetimes that lead to observed phenomena like finite thermal conductivities. Phonons are also known to play a role in electrical resistivity. Electronic carriers can scatter to generate phonons that can increase the material temperature.

Furthermore, although the QHA improves the accuracy of thermodynamic models to account for experimental thermal expansion, it is not an entirely rigorous approach consistent with the underlying physics of the material.

Another issue is that the potentials between atoms are not truly quadratic. This is evident because as two atoms get farther away from each other, their attractive force decreases, indicative of a long range $1/r$ potential.

In perturbation theory, we can further expand the potential to keep higher order terms. We can use a second quantization expression for the atomic displacements to determine the Hailtonian of any order in this second quantization form. We can see, in the Hamiltonian, how phonons interact through the creation and annihilation operators. It is often common to expand to keep both the cubic and quartic terms.

Experimental characterizations of phonons at high temperatures are extremely important to elucidating the consequences of the anharmonicity in materials. At high temperatures more of the anharmonic portions of the potentials are explored, so it makes sense that we

more readily see these anharmonic effects.

More concretely, anharmonic phonon-phonon interactions affect the observed phonon spectra by not only broadening, but also shifting their absolute energies. This can be apparent in measurements of both phonon dispersions and DOS.

The consequences of anharmonicity vary from material to material, with some materials displaying very little anharmonic softening and broadening. It is not entirely clear which materials are able to be well characterized under only the QHA and which materials need ample assistance from anharmonic effects. Understanding the validity, or invalidity, of the QHA for the element Germanium is the focus of much of this thesis.

We must now pray to the neutron gods.

Camille Bernal and Claire Saunders

3

Phonon Anharmonicity in Germanium from 296 to 1203 K

3.1 Motivation and Goals

Materials expand as the ambient temperature increases. We call this thermal expansion. Thermal expansion can be best understood as how the free energy, $F = E - TS$, depends

on volume. For any given temperature, a material will expand if its free energy is lower at a larger volume. Thermal expansion creates a force against the hypothetical springs keeping atoms together, increasing the E term in the free energy. This expansion will force against the springs, increasing the E term in the free energy. However, there may be a gain in the temperature multiplied by entropy (TS), which allows for the free energy to be reduced. To find the optimal volume we minimize $\frac{\partial F}{\partial V}$.

We can further write,

$$\frac{\partial F}{\partial V} = -P = \frac{\partial E}{\partial V} - T\frac{\partial S}{\partial V}. \tag{3.1}$$

Therefore, if $P = 0$,

$$T\frac{\partial S}{\partial V} = T\frac{\partial E}{\partial V}. \tag{3.2}$$

The left hand side is approximately the elastic pressure and the right hand side is often called a thermal pressure. To find $V(T)$ we end up having to balance the elastic pressure with the entropy change with V (and T).

We are therefore very interested in understanding how the entropy of a material varies with V and T. We had previously noted in Chapter 2 that most of the entropy stems from the vibrational entropy of phonons. We had also noted that the phonon entropy contribution, and the phonon contribution to other relevant thermodynamic quantities, can be calculated from the density of states, which is essentially a spectrum of phonon frequencies. These phonon frequencies shift in both the quasiharmonic and anharmonic model, as described in the previous chapter.

Understanding how and why this spectrum of phonon frequencies varies as a function of volume and temperature not only allows us to calculate $S_{vib}(V, T)$, but also gives us a deeper

understanding of the origins of thermal expansion. Let us examine the phonon frequencies more closely.

We can write the frequency, ω, as a function of volume and temperature. Volume tells us generally how far apart the atoms are, which of course, affects the potential in the hypothetical springs between atoms. Temperature tells us how far the atoms move about their initial equilibrium positions. Expanding $\omega = \omega(V, T)$ to first order yields

$$d\omega = \left(\frac{\partial \omega}{\partial V}\right)_T dV + \left(\frac{\partial \omega}{\partial T}\right)_V dT \tag{3.3}$$

The first term in the expansion is related to the Gruneisen parameter, which we discussed before in Chapter 2. We rewrite the Gruneisen parameter, γ, here as,

$$\gamma \equiv -\left(\frac{V}{\omega}\frac{\partial \omega}{\partial V}\right)_T \tag{3.4}$$

The next term is related to the anharmonicity parameter, which is essentially the fractional change in frequency as a function of temperature. We define the anharmonicity parameter as,

$$\mathcal{A} \equiv -\left(\frac{1}{\omega}\frac{\partial \omega}{\partial T}\right)_V \tag{3.5}$$

These two definitions allow us to separately think about the two theories we discussed in the previous chapter. In a purely quasiharmonic theory, the phonon modes are harmonic, but their frequencies must be shifted with volume. The only role of temperature is to expand the volume. The frequencies would therefore shift the same way if the volume change was induced by varying the ambient pressure instead of the temperature.

A purely anharmonic theory, on the other hand, has frequencies that are only dependent on the temperature. Even if the volume remains fixed, the frequencies shift due to the increased excursion distance of the atoms about their equilibrium positions, leading to phonon-phonon interactions.

Usually, however, we have both quasiharmonic and anharmonic contributions to the shifting frequencies, so we write $\omega(V(T), T)$. The big question is then, for any material, what are the relative effects to the phonon frequencies of quasiharmonicity and anharmonicity? Can we characterize a material as more quasiharmonic-like or more anharmonic-like?

In an ideal world, we would like to be able to say that materials with certain properties exhibit high levels of anharmonicity, while others with other properties exhibit high levels of quasiharmonicity instead. This is not the case in the real world. It is often hard to get a sense of how a material will behave before doing computational or experimental studies.

In this thesis we examine the deviations from harmonicity of Germanium, an element with atomic number 32. Ge is a hard-brittle, lustrous, grayish-white metalloid. It is in group 14 and period 4 on the periodic table. It is chemically similar to its two neighbors, tin and silicon. The thermal properties of Ge are important for uses in fiber-optic systems, solar cell applications, light emitting diodes, and infrared optics.

Both the quasiharmonic and anharmonic approximation predict shifts in phonon frequencies. We would like to understand the role of both quasiharmonic and anharmonic effects in generating these frequency shifts.

Before proceeding, it is important to note a common misconception about phonon theory. It is frequently stated that we can sufficiently use a harmonic model at low temperatures, a quasiharmonic model at moderate temperatures and an anharmonic model at high

temperatures. The issue here is, usually, the frequency shifts from quasiharmonicity, due to expansion of the volume, grow linearly with temperature. In anharmonic theory the predicted frequency shifts are also linear with temperature. This means that if anharmonicity dominates at high temperature, then it will dominate at all temperatures (fig 3.1). It is therefore not so simple as using a specific theory at a specific temperature. The real, fundamental question is which one dominates at all temperatures.

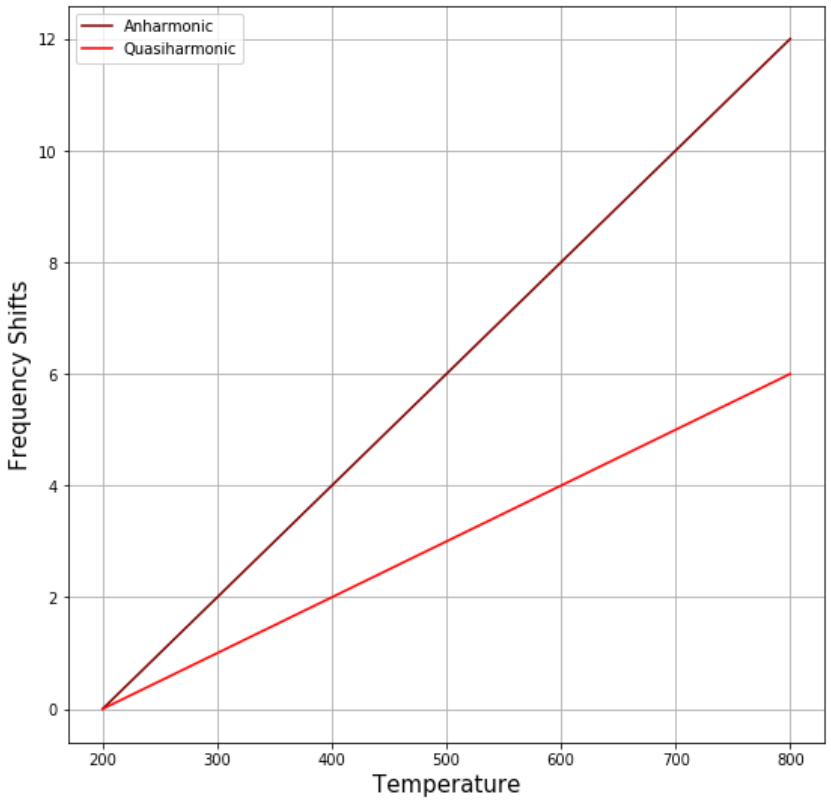

Figure 3.1: Illustration idea from Prof. Brent Fultz. Note that if anharmonicity dominates the contribution to the frequency shifts at high temperatures, it does so at all temperatures as well.

There is one redeeming quality, however, about the prior misconception. It is that anhar-

monic effects, if they exist, will definitely be more noticeable at higher temperatures. In fig 3.1 it is clear that the difference in delta omega between the two theories is greater at higher temperatures. High temperature studies of phonon behavior are therefore critical to our understanding of the role of anharmonicity in materials.

High temperature studies are also important because most of the entropy of materials stems from phonons. We can recover the phonon contribution to thermodynamic quantities from the density of states. For example, in eq. 2.29 we used it to calculate the vibrational entropy. We would like to determine how this phonon contribution varies as a function of temperature. Recall that eq. 2.29 was actually derived using the harmonic approximation. It assumed, however, that we would have accurate densities of states (spectrum of phonon frequencies), even at higher temperatures.

A naive method of calculating S_{vib} at higher temperatures would therefore be to keep the density states constant as temperature increases, and rely solely on the Plank distribution to generate the changes in S_{vib}. A better method would be to actually experimentally determine the phonon DOS at higher temperatures, and substitute that in for g(e) in equation 2.29. This would allow us to determine the accurate contribution of S_{vib} to the total entropy. This has indeed been done for several materials at lower temperatures, including germanium. It is therefore well known, at least at low to moderate temperatures [7], that most of the entropy of materials stems from S_{vib}. This was discovered partly through previous experimental work that employed INS to study the low to moderate temperature lattice dynamics, but to our knowledge, there has not been an INS study of phonons in Ge up and through the melting point.

Our understanding of the phonon spectra at high temperatures is still emerging. In this

section of the thesis we present an analysis of the Ge phonon spectra at temperatures up to 1203 K. To reiterate, the merits of this high temperature analysis are two-fold. It will 1: allow us to better differentiate and elucidate the quasiharmonic and anharmonic contributions to the softening of phonon frequencies (because these differences are more apparent at high temperature) and 2: allow us to test whether or not the statement that most of the total entropy in Ge can be accounted for by harmonic-theory-derived vibrational entropy remains valid at higher temperatures.

3.2 Experimental Setup

Inelastic neutron scattering (INS) measurements were performed on a curved polycrystalline/powder sample of Ge with the time-of-flight Wide Angular-Range Chopper Spectrometer (ARCS) at the Spallation Neutron Source (SNS) at Oak Ridge National Laboratory (ORNL).

Ge was pulverized and sealed into high purity quartz ampoules. The effective sample thickness was 5.0 mm. The quartz ampoules were then contained in a vanadium foil sachet. The sachet was mounted by a wire so that it hung in the sample area of the spectrometer in a low-background electrical resistance vacuum furnace.

The incident energy was 50meV, and the sample temperatures ranged from 298-1211K. For this thesis we examine measurements of phonon spectra taken at 296, 323.15, 600.15, 773, 873, 973.15, 1073.15, 1173.15, and 1203 K. Background measurements were taken on empty quartz ampoules in the same vanadium foil sachet at corresponding temperatures.

3.3 Time-of-Flight Methods

The incredible phonon spectra we obtained would not be possible without the newest advancements in INS technology available at ARCS. Time-of-flight instruments are often the way to go when it comes to studying the phonon DOS for materials. These allow us to see all the phonons within a material. This is quite different from older methods where we used to use a triple-axis spectrometer to collect phonon dispersion curves point-by-point.

The SNS at the Oak Ridge National Laboratory is shown in fig. 3.2. A beam of protons is used to generate neutrons by spallation. We first start with hydrogen ions with extra electrons produced from an ion source. These ions are formed into a beam with some time structure associated with it. The beam is accelerated to around 1 GeV by a linear accelerator. After a foil strips the ions of their extra electrons, the beam is bunched even further by passing it through an accumulator ring. This refines the time structure to pulses that are 1 μs at 60 Hz. These proton pulses then strike a liquid mercury target, spalling neutrons in the process. We can set the wavelength of these neutrons by allowing them to come into equilibrium with baths of different temperatures. For example, we could let them come into equilibrium with water to produce thermal neutrons, or we could let them come into equilibrium with liquid hydrogen to produce cold neutrons. The wavelength of these neutrons essentially sets the granularity they can resolve in materials. These neutrons are then, of course, scattered off our sample to probe the vibrational lattice dynamics.

The initial energy, E_i and initial wavevector, Q_i, are determined mainly through careful calculations of timing. In a direct-geometry, time-of-flight chopper spectrometer, like in fig. 3.3, the timing of each neutron pulse is known. We use two types of choppers to control

Figure 3.2: An aerial image of the SNS at Oak Ridge National Laboratory

the neutrons. T_0 choppers stop γ-rays and high speed neutrons from leakage. The Fermi chopper provides us with our chromatization. Neutrons that are too fast or slow don't make it through the pair of choppers, so in this way we are able to modulate the initial conditions of the incoming neutrons.

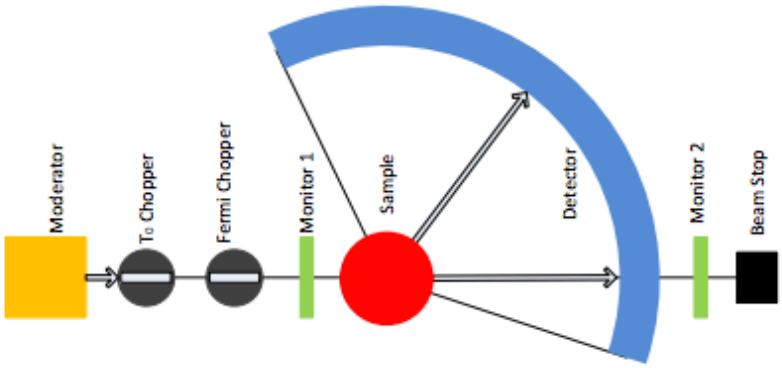

Figure 3.3: A schematic of a direct geometry in a time-of-flight neutron chopper spectrometer.

The neutrons that are able to get through the choppers are scattered off our sample. These scattered neutrons ultimately arrive at our detectors, where their arrival times and positions

are recorded (see fig. 3.4). The detectors are typically packs of long tubes containing ^3He. The metadata associated with each neutron is its detector, detector pack, pixel, and arrival time. We then calculate the neutrons' final wavevectors and energies as,

$$E_f = \frac{m_n}{2}\left(\frac{L}{\tau}\right)^2 \tag{3.6}$$

$$Q_f = \frac{m_n L}{\hbar\tau}, \tag{3.7}$$

where L is the distance from the detector pixel to the sample and τ is the arrival time. The unit vector in the direction of the vector connecting the sample to the pixel encapsulates the direction associated with Q_f. The energy transferred to the sample is then, $E = E_i - E_f$ While the wavevector is $Q = Q_i - Q_f$.

In this experiment on Ge we make use of a polycrystalline sample. This has the effect of allowing us to neglect the direction of Q. The neutron scattering is instead averaged over all directions with the same magnitude.

3.3.1 Sampling Region

Time-of-flight techniques allow us to sample large regions of q-space (reciprocal space) simultaneously. Collecting data over such a large span of reciprocal space is one of the main advantages of time-of-flight techniques over triple-axis spectrometers. Through time-of-flight we are able to do phonon counting to reveal underlying thermodynamic quantities. For a particular scattering angle, φ and incident energy, E_i, the maximum momentum transfer Q_{max}

and the energy transfer can be related by,

$$Q_{max} = \left(\frac{1}{2.071} \left(2E_i(1 - cos(\varphi)\sqrt{1 - \frac{E}{E_i}} - E \right) \right)^{\frac{1}{2}} \tag{3.8}$$

This is known as the kinematic limit. This range of Q usually covers several tens of Brillouin zones. We can achieve high Q by measuring phonons at larger scattering angles or simply by using higher incident neutron energies. The issue with the latter is that it will degrade the energy resolution. The issue with the former is that the instrument resolution may not be high enough to accommodate it. We also often face lower signal-to-noise ratios at higher Q because multiphonon and multiple scattering effects tend to be stronger.

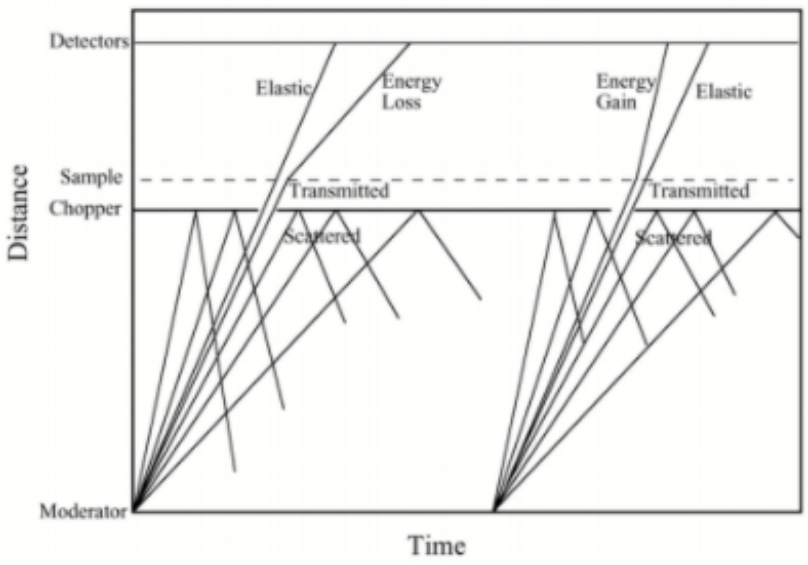

Figure 3.4: A distance vs time plot of the chopper timing. From [2]

3.4 Calculating the S(Q, E)

Recall that for our experiment, the incident energy was 50meV, and the sample temperatures ranged from 298-1211K. Measurements were taken on both pulverized Ge samples and on empty samples (just the quartz ampoules). The raw data had to be reduced to plots of intensity as a function of momentum and energy transfers, also known as the dynamic structure factor, S(Q, E). Much of this thesis was devoted to understanding and implementing code to reduce the raw data from INS experiments to the dynamic structure factor. The data reduction was performed with DGS in Mantid .

Reducing the raw data is a fair bit of work. At a minimum we must perform the following operations [2]:

- Efficiency corrections and detector masking
- Determination of the indecent energy
- Data normalization
- Removal of background scattering

We should also account for multiple scattering here as well (when a single neutron scatters more than once) because this type of scattering involves the geometry of the instrument and should therefore not be included in an accurate S(Q, E). We instead skip this step for now and couple it with multiphonon scattering (when a single neutron produces more than one phonon) while recovering the phonon DOS.

A very detailed account of the above steps can be found in (http://docs.danse.us/DrChops/ExperimentalInelasticNeutronScattering.pdf).

We highlight some of the most important points below. The ^{3}He detectors used for neutron scattering may not always be working properly all the time. For example, some may be quite noisy and others may go completely silent. The detectors that do not fit our specific requirements must be identified and masked. We do this by setting a threshold neutron count minimum and maximum for each pixel. The mask removes pixels for which the neutron count is outside the bounds we set. The bounds are often set by trial-and-error. We must look to ensure that bad detectors are thrown out without vanishing the relevant dispersions in our dynamic structure factor.

The efficiency of the detectors is prescribed coordinates (d, p, and t) where d is the detector, p is the pixel and t is the time-of-flight. The efficiency from one detector to the next is not always constant. We can often correct for detector efficiency by using a measurement from an element that is a highly incoherent neutron scattering.

Furthermore, the high flux from the SNS allows for calibrations to be done at the pixel level. This can accommodate for efficiency variations within a detector. We divide the measured intensity by the efficiency to determine the calibrated intensity,

$$I_{dpt} = \frac{I^0_{dpt}}{\gamma_{dpt}}. \tag{3.9}$$

ARCS uses multiple detector banks to cover a solid angle of about π steradian. This large solid angle means that pixels at different detectors and even different positions within a single detector will cover varying levels of solid angle. These varying levels must also be calculated and corrected for.

Although we stated before that the incident neutron energy is known, we often calculate it again from our data to get a more accurate value. We can do this by fitting the elastic peak

of our scattering data to a gaussian or similar function.

As the scattered neutrons are detected, they are binned to calculate S(E, 2θ), where 2θ is the scattering angle and E is the energy transfer. We normalize by the proton current on the liquid mercury target. We then rebin S(E, 2θ) to S(Q, E). It is often common to use 0.5 meV per energy bin and 0.1 Å per momentum bin. Note that this should technically be I(E, 2θ) instead of S(E, 2θ) because we have not yet corrected for multiple scattering.

We calculated the dynamic structure factor from the raw data for all the measurements taken on Ge. In this thesis, because we ultimately needed the phonon DOS at all temperatures, we calculated the S(Q, E) at all temperatures as well. Below we present the calculated S(Q, E) at both the lowest and highest temperatures that measurements were taken at. We perform background subtraction in the next section.

3.5 S(Q, E) to Phonon DOS

Another large portion of this thesis was devoted to calculating the phonon density of states from the S(Q, E). This is probably the most exciting step apart from the analysis of results, simply because how informative the phonon DOS is with respect to the underlying physics (see Chapter 2).

The data that we are interested in is that which is away from the zero energy transfer line. From fig. 3.5 and 3.6 a distinct elastic line from Bragg scattering can be seen as the prominent yellow/green line down the middle. Inelastic scattering can be seen in the dispersions above and below the elastic scattering line. The first step is therefore to remove the elastic peak below a certain energy transfer. To subtract this elastic peak we assume the intensity of the

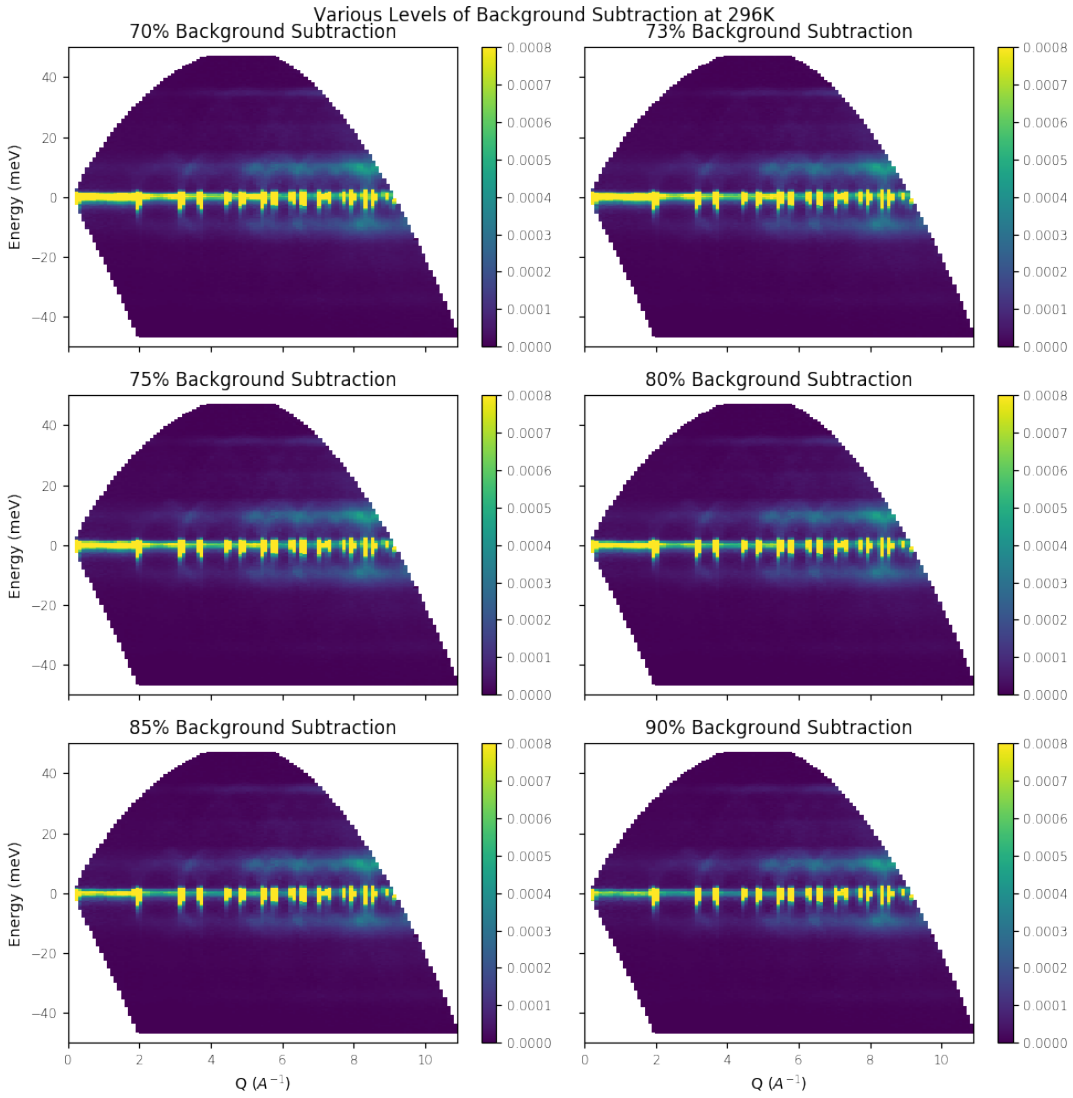

Figure 3.5: Various levels of background subtraction at 296 K

phonon DOS scales as E^2 and fit the elastic peak to a Gaussian. Below is a figure plotting the isolated elastic peak for Ge at 296 K.

To recover an accurate phonon DOS we must ensure we calculate a one-phonon DOS, which is obtained after correcting for multi-phonon and multiple scattering. Again, multi-

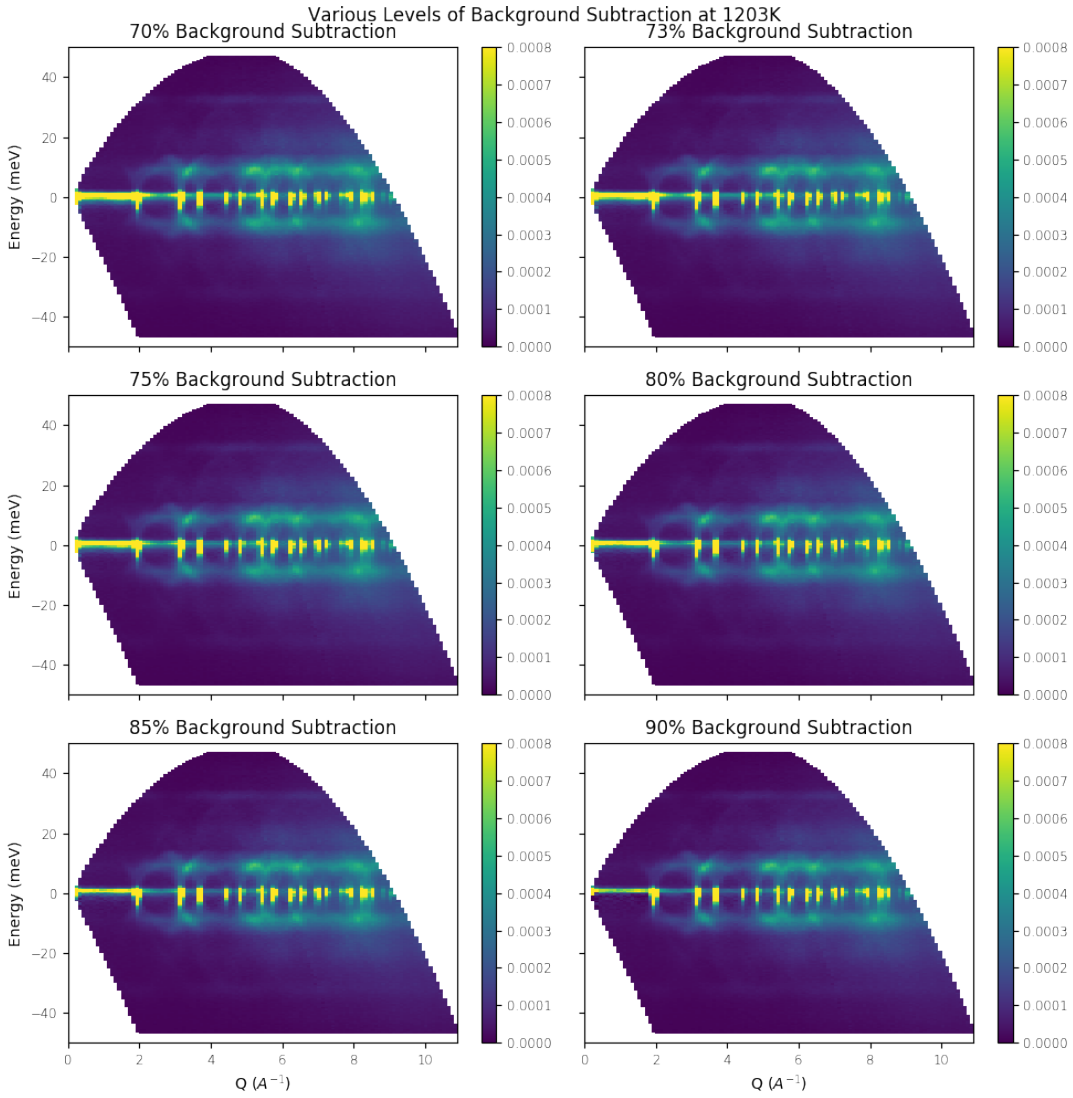

Figure 3.6: Various levels of background subtraction at 1203 K

phonon scattering is scattering from a single neutron that creates more than one phonon. Multiple scattering is scattering from a single neutron scattering more than once before leaving the sample. If we had a simple resolution function and did not deem the effects of multiple scattering too relevant, we could make use of the Fourier-log method. We instead chose

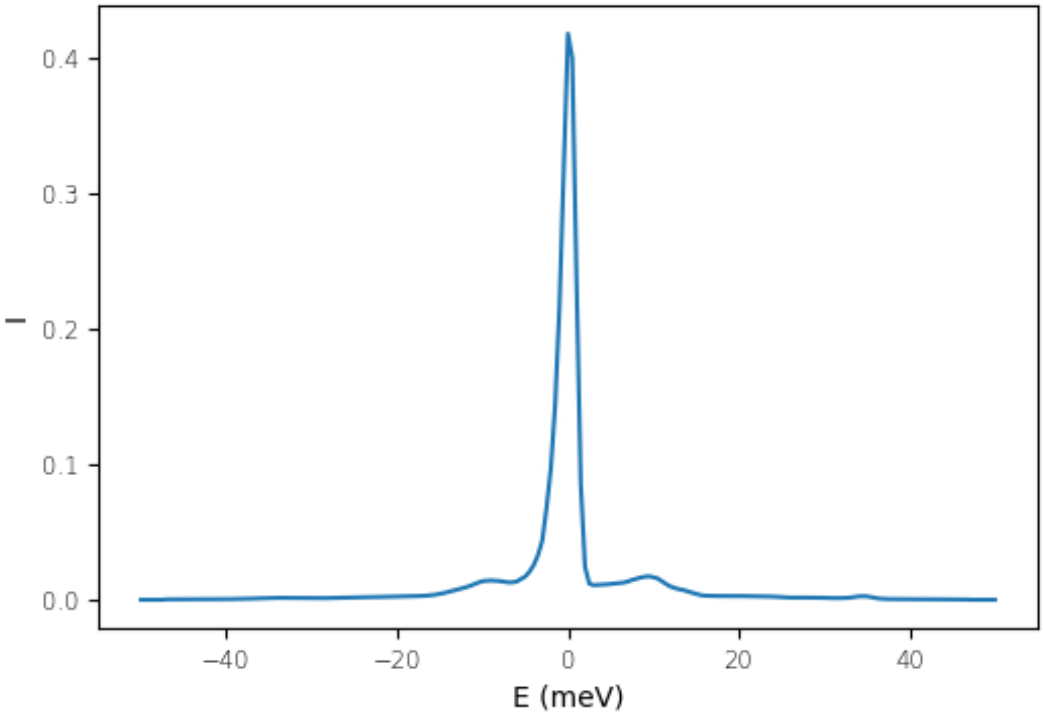

Figure 3.7: Total elastic peak from 296 K

to use an iterative method, which is more accurate for time-of-flight chopper neutron spectrometers.

For both multiple and multiphonon scattering, a two-scattering profile is simply the convolution of two single scattering-profiles. We can then relate an n-phonon-scattering profile to a one-phonon-scattering profile through the following recursion,

$$P^n(E) = \int_{-\infty}^{\infty} P^{n-1}(E')P^1(E - E')dE' \tag{3.10}$$

Where $P^n(E)$ is the n-phonon-scattering profile and $P^1(E)$ is the one-phonon-scattering profile. It is believed that slowly varying functions of Q and E relate the multiple scattering

to the multiphonon scattering. Approximating these slowly varying functions as constant with respect to Q and E allows us to represent the total intensity as,

$$I(Q,E) = N' \sum_{n=1}^{\infty} (1 + a_n) S^n(Q,E) \tag{3.11}$$

The A_n's are the slowly varying functions which we have approximated as constant. $S^n(Q,E)$ is the n-phonon-scattering and the N' is a normalization constant. We assume that the A_n's are the same for all $n > 2$. We also assume that the incoherent approximation applies. This yields for the intensity,

$$I(Q,E) = N(S^1_{inc}(Q,E) + (1 + C_{ms}) S^{2+}_{inc}(Q,E)) \tag{3.12}$$

Where,

$$S^{j+}(Q,E) = \sum_{n=j}^{\infty} S^n(Q,E) \tag{3.13}$$

$$C_{ms} = \frac{1 + a_2}{1 + a_1} - 1 \tag{3.14}$$

$$N = N'(1 + a_1)(1 + \frac{\sigma_{coh}}{\sigma_{inc}}) \tag{3.15}$$

The value of C_{ms} is not known beforehand. Instead, a series of phonon DOS is generated from a set of possible values. We then solve for the DOS with equation (previous big one) at each of the possible values of C_{ms}. We then select the best DOS from those generated with different C_{ms} by minimizing a penalty function. The procedure of recovering the single

phonon DOS is implemented using the getDOS function in the multiphonon package [8]. More details, such as the nature of this penalty function, can be found in [2] for the interested reader.

In simple terms, the main steps of getDOS are as follows. We first start with an initial guess of the DOS. We then calculate the SQE of multiphonon scattering before calculating the SQE of multiple scattering. The multiple scattering and multiphonon scattering SQE are subtracted from the experimental SQE to obtain an approximation of the single phonon SQE.

A new DOS is computed from this single phonon SQE. We then compare the new DOS to the initial guess for the DOS and compare the difference. If the difference is above some threshold, we continue iterating, but remember to substitute the new DOS as the initial guess for the next iteration round. If the difference is below our threshold, we keep the new DOS.

We calculated one-phonon DOS's for each of the S(Q, E)'s we found in the previous section. The S(Q, E)'s for each temperature, along with their respective DOS are displayed below.

3.6 Results

In the motivation section to this chapter we mentioned that we would like to understand the quasiharmonic and anharmonic contributions to the softening of phonon frequencies in Ge. In the quasiharmonic theory the softening is only caused by changes in volume. The softening of a purely quasiharmonic material is therefore usually not as pronounced as the softening from a material that experiences both quasiharmonic and anharmonic effects. Essentially,

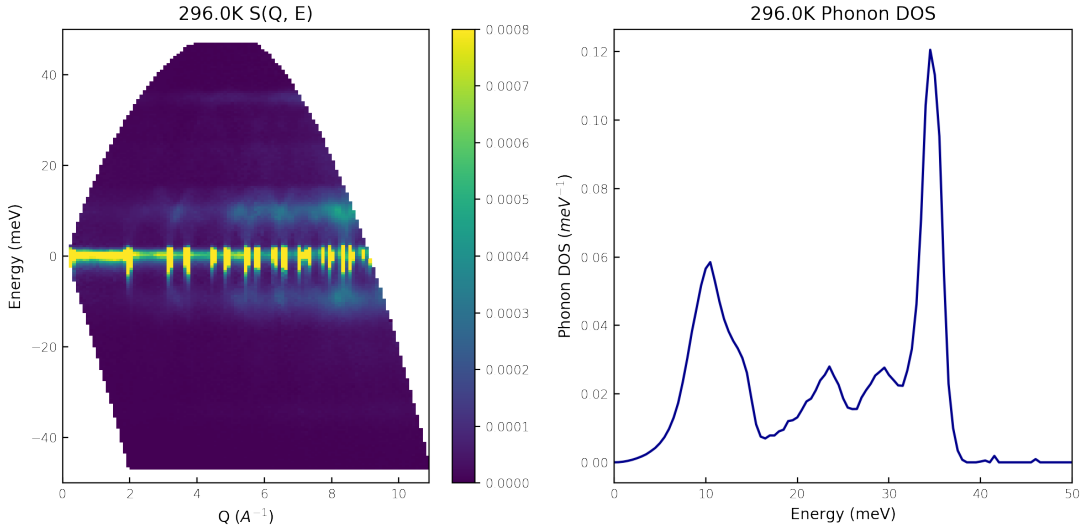

Figure 3.8: S(Q, E) and Phonon DOS for Ge at 296 K

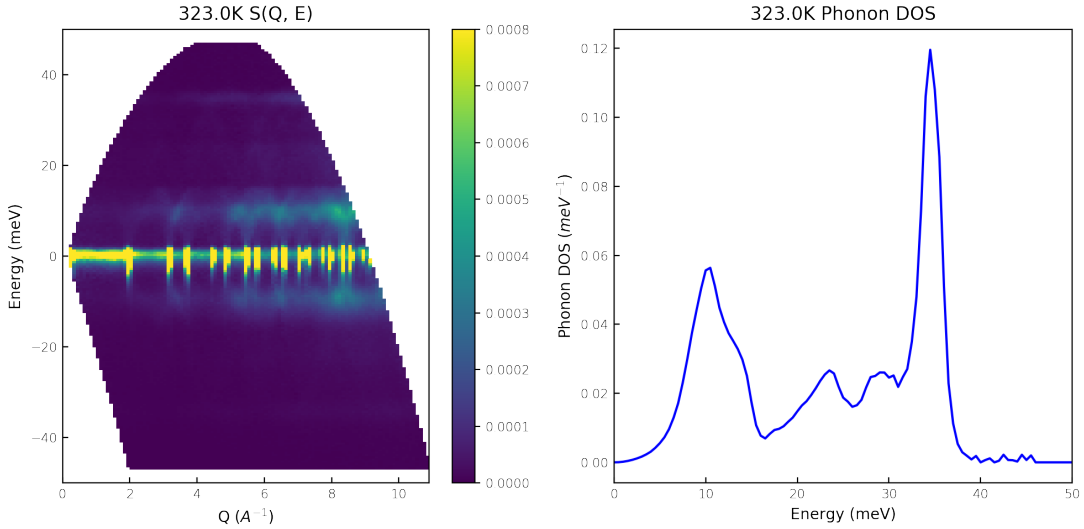

Figure 3.9: S(Q, E) and Phonon DOS for Ge at 323 K

the temperature dependence of ω in the anharmonic theory allows for greater phonon softening from the phonon-phonon interactions as atoms deviate away from their equilibrium

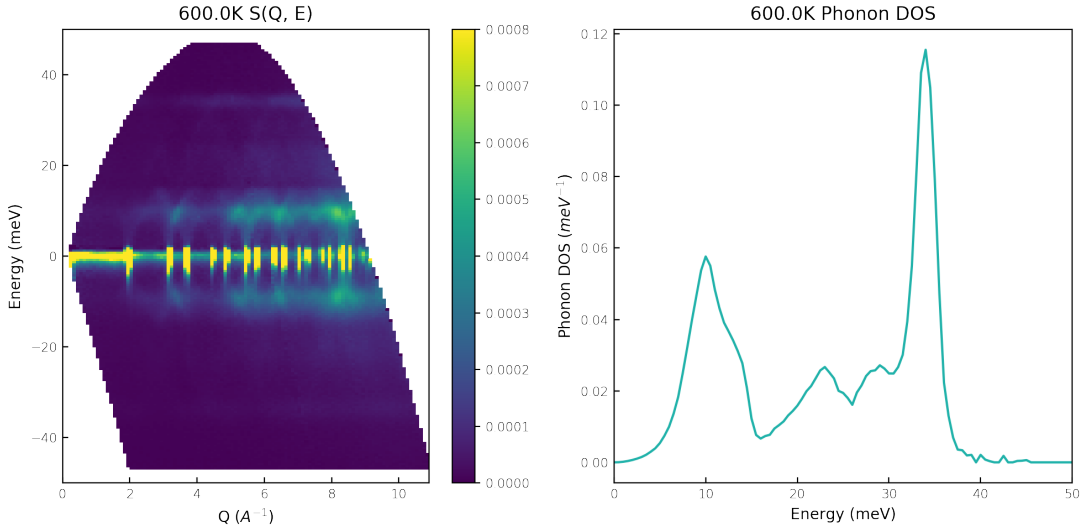

Figure 3.10: S(Q, E) and Phonon DOS for Ge at 600 K

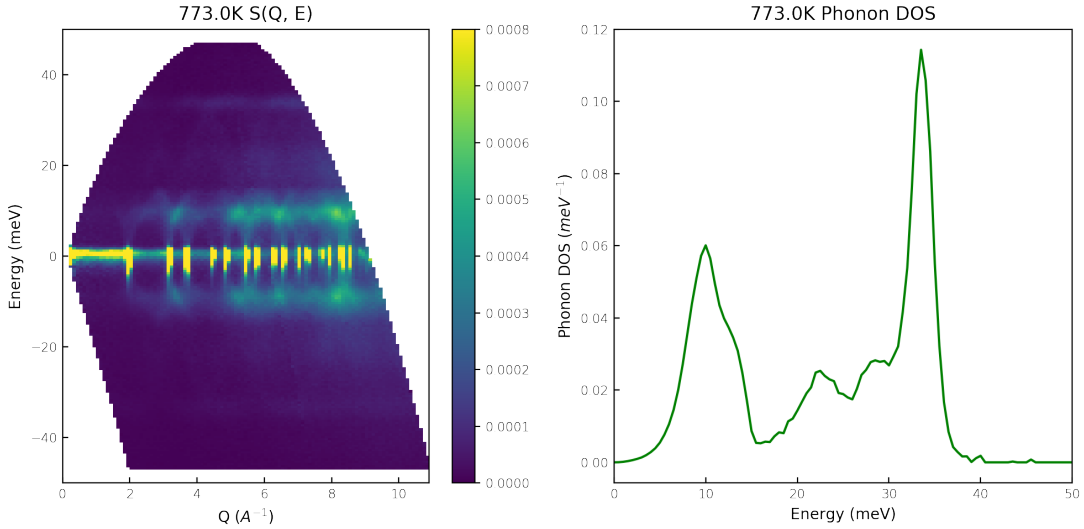

Figure 3.11: S(Q, E) and Phonon DOS for Ge at 773 K

positions. These interactions are more prominent at higher temperatures as atoms are able to deviate farther away.

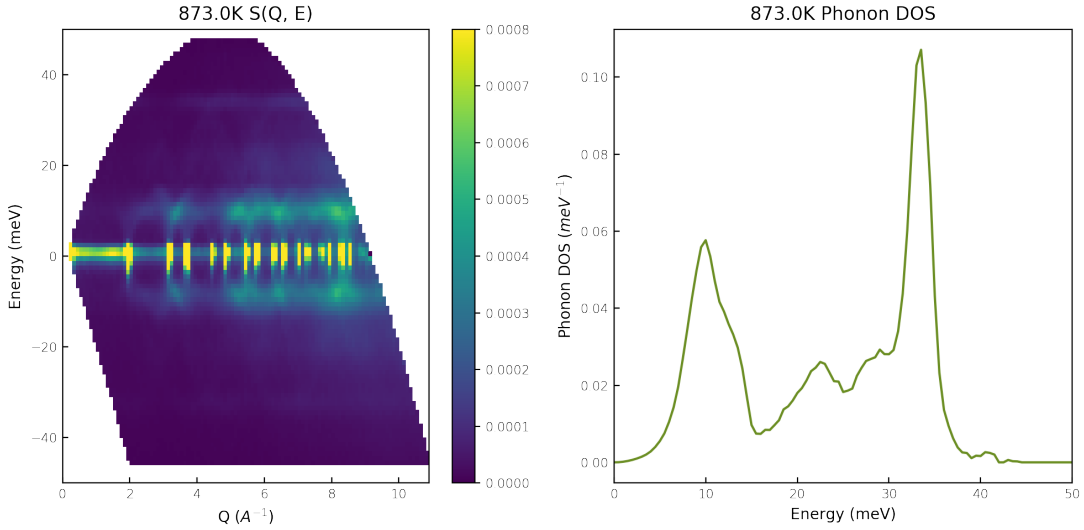

Figure 3.12: S(Q, E) and Phonon DOS for Ge at 873 K

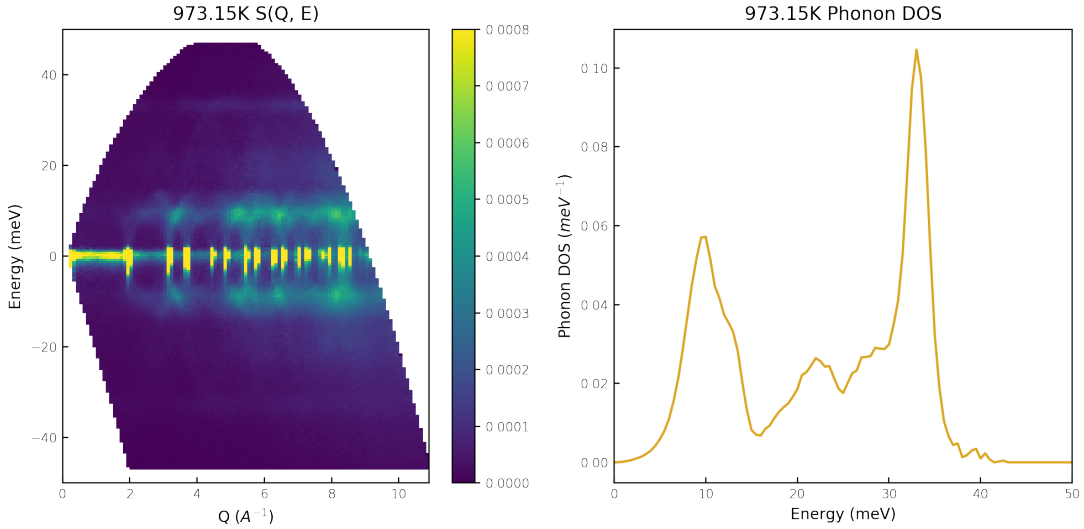

Figure 3.13: S(Q, E) and Phonon DOS for Ge at 973.15 K

Plotting the phonon DOS we calculated in the previous section all on one plot allows for a clear visualization of the phonon softening (fig. 3.17).

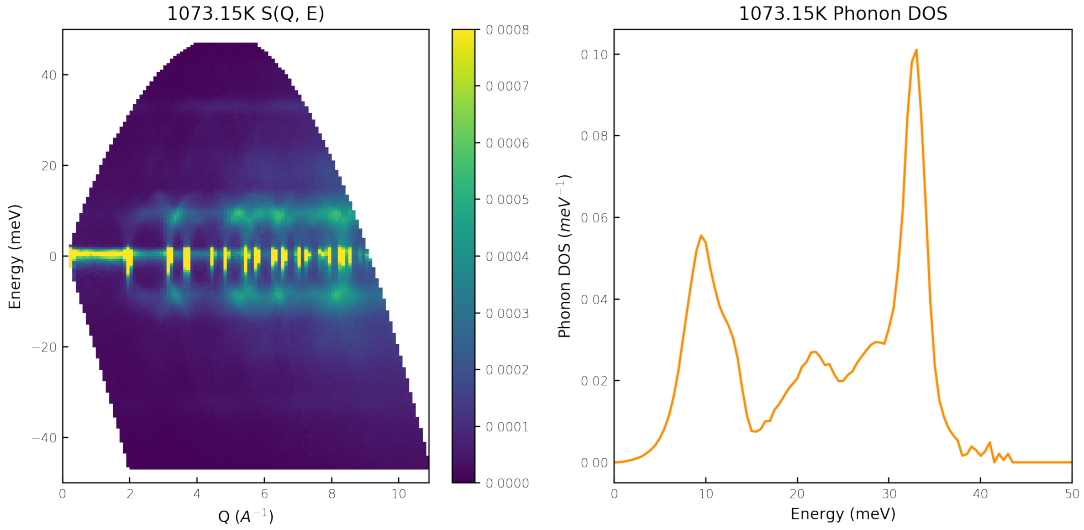

Figure 3.14: S(Q, E) and Phonon DOS for Ge at 1073.15 K

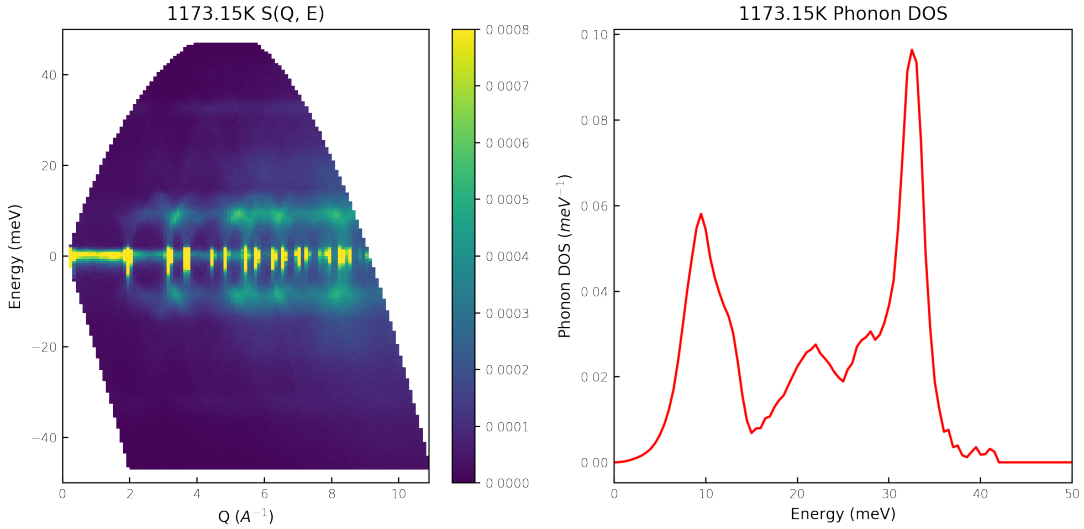

Figure 3.15: S(Q, E) and Phonon DOS for Ge at 1173.15 K

There is a sharp cutoff in the phonon spectrum at 41 meV. The fact that the phonon DOS almost vanishes above the cutoff reassures us of the validity of our corrections for back-

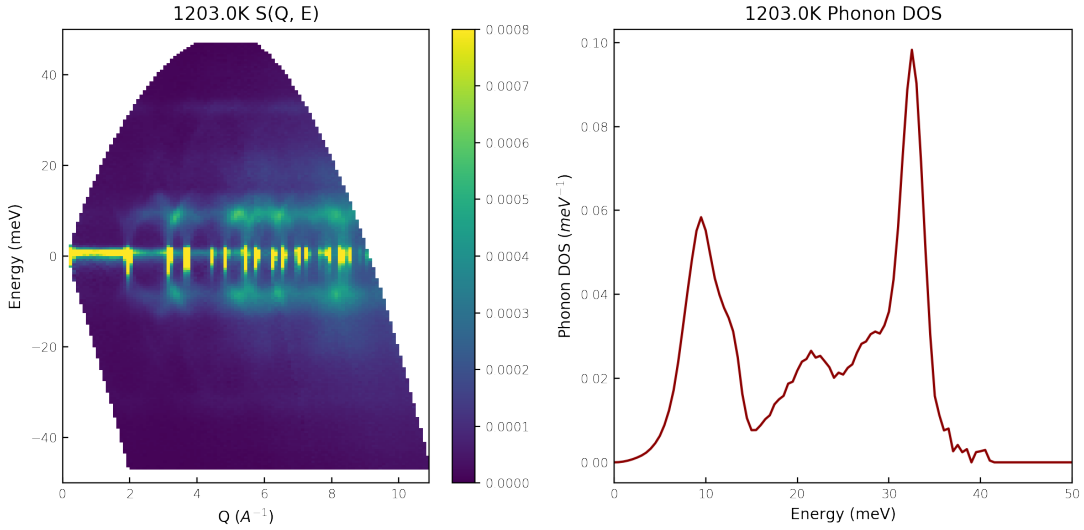

Figure 3.16: S(Q, E) and Phonon DOS for Ge at 1203 K

ground, multiple, and multiphonon scattering. Thermal softening of all the modes is immediately evident, especially for the highest energy mode. All the modes gradually decrease in energy as the temperature increases. It is interesting to note that this effect propagates well into the higher temperatures, all the way up to 1203 K. We also observe a distinct broadening of the modes as temperature increases.

Solids with more than a single atom per unit cell, like Germanium, give rise to two types of phonons, lower energy acoustic phonons, and higher energy optical phonons. Acoustic phonons are coherent movements of the atoms out of their equilibrium positions. Since acoustic phonons mostly present a linear dispersion relationship, especially at lower values for the wavevector, we can often model them by Debye-like dispersions. Optical out-of-phase movements of the atoms in the lattice. We can sometimes model these by Debye-like dispersions because of their somewhat constant dispersion relation.

Both types of phonons can have transverse and longitudinal modes. There are two trans-

verse directions and one longitudinal direction. We therefore expect 6 different modes to be present in our phonon DOS. We initially attempted to fit all the phonon DOS to 6 Gaussians. We found that it was difficult to resolve the highest energy transverse optical mode from the longitudinal optical mode. The energies were so similar to each other, indicating some mixing between the modes. We also attempted to fit the phonon DOS to 6 Lorenzian functions and 6 Voigt profiles. We faced similar issues. We instead decided to fit 5 Gaussians instead. This is quite a standard method for accounting for phonon modes with similar energies.

Gaussian fits were done for each of the phonon DOS. As an example we show the Gaussian fits overlaying the data for the 1203 K DOS (fig. 3.18). We also make note of the centers of these Gaussians. We define these centers as the positions of the peaks for our analysis of the peak shifts.

The accuracy of the fits is evident once overlaying the sum of the 5 Gaussians with the actual data. The 5 phonon modes are apparent in all the phonon DOS. For example, we may examine the DOS at 1203 K. The two transverse acoustic modes are at 9.04 meV and 10.24 meV. The longitudinal acoustic mode forms the first shoulder in the middle of the graph at 20.75 meV. The lower energy transverse optical mode forms the second shoulder at 29.43 meV. Finally, the higher energy transverse and longitudinal optical modes form the rightmost peak at 33.60 meV.

With the locations of the peaks for each of the phonon DOS we can quantify the level of phonon softening by calculating the fractional shifts in the peak frequencies. We can label each of the 5 phonon modes by an index, i. We define the fractional shift ζ of the ith phonon

mode at temperature T as,

$$\zeta_{T,i} = -\frac{E_{T,i} - E_{296K,i}}{E_{i,296K}} \tag{3.16}$$

The negative sign out front is there because all the fractional shifts are negative, so the negative sign makes the fractional shift positive. We calculate the fractional shift of the ith mode at each temperature to quantify the magnitude of the phonon frequency shifts as a function of temperature. We then do this for each of the 5 phonon modes. The result is a quantitative picture of the frequency shifts of each of the phonon modes as a function of temperatures (fig. 3.19).

The points represent the frequency shifts at each temperature for each mode. We have labeled and color coded each of the modes for clarity. We have also plotted each mode with different symbols for further clarity.

3.6.1 Error Propagation Aside

In performing the gaussian fits to each of the DOS we made sure to maintain the covariance matrix for each of the fits. For each temperature, the square root of the diagonal of the covariance matrix provides the standard deviation of each of the peak positions. We then perform the standard method of error propagation by Taylor expanding our formula for the percent fractional shift. In this first order approximation, if some function Q is some combination of sums and differences $Q = a + b + ... + z$, then

$$\delta Q = \sqrt{(\delta a)^2 + (\delta b)^2 + ... + (\delta z)^2} \tag{3.17}$$

If,

$$Q = \frac{ab...c}{xy...z} \tag{3.18}$$

,

then,

$$\frac{\delta Q}{|Q|} = \sqrt{\left(\frac{\delta a}{a}\right)^2 + \left(\frac{\delta b}{b}\right)^2 + ... + \left(\frac{\delta z}{z}\right)^2} \tag{3.19}$$

Using the above approximation, we note that eq. 3.16 is simply the composition of an addition with a multiplication. This then lets us calculate the error associated with each of the frequency shifts. These errors are illustrated with error bars in fig. 3.19.

3.7 Results cont.

We then perform a linear regression on each of the plots of frequency shift as a function of temperature. We overlay the results of this linear regression for each phonon mode.

It is interesting that the lower energy transverse optical mode has a slope much lower than the rest of the modes. Besides this mode, the modes follow the trend that the lower energy modes have a higher slope than the higher energy modes. This means that, in general, the largest fractional changes are found for the lower energy modes. The largest fractional change is for the low-energy transverse acoustic mode. This seems to indicate that lower energy modes are still able to experience thermal softening, interestingly at the highest rate, even given their low initial energies.

This analysis does not yet give us an understanding of the contributions to the deviation from harmonicity in Ge. Both the QHA and anharmonic theory predict thermal softening.

Can we say that all the thermal softening is due to quasiharmonic effects? Do we need to admit some anharmonicity is at play here? For a quantitative explanation we turn to the Gruneisen parameter. We previously defined the mode Gruneisen parameter in terms of frequency shifts in eq 2.32. Since $E = \hbar\omega$, we can identically define the mode Gruneisen parameter as

$$\gamma_i = -\frac{V}{\varepsilon_i}\frac{\varepsilon_i}{\delta V} \tag{3.20}$$

This represents the fractional shift in energy of phonon mode i per fractional shift in volume. We can further define a mean Gruneisen parameter as

$$\bar{\gamma} = -\left\langle \frac{V}{\varepsilon_i}\frac{\Delta\varepsilon_i}{\partial V} \right\rangle = -\left\langle \frac{\partial \ln \varepsilon_i}{\partial \ln V} \right\rangle \tag{3.21}$$

This acts to the average the thermal behavior of the phonons in the whole Brillouin zone. We can define isothermal (γ_P) and isobaric (γ_T) Gruneisen parameters as,

$$\bar{\gamma}_P = -\frac{1}{3\alpha(T)}\left\langle \frac{\partial \ln \varepsilon_i}{\delta V} \right\rangle\Bigg|_T \frac{\partial V}{\partial T} = B_T \left\langle \frac{\partial \ln \varepsilon_i}{\partial P} \right\rangle\Bigg|_T \tag{3.22}$$

and

$$\bar{\gamma}_T = -\frac{1}{3\alpha(T)}\left\langle \frac{\delta \ln \varepsilon_i}{\delta T} \right\rangle\Bigg|_P \tag{3.23}$$

.

The isothermal Gruneisen parameters describe the phonon energy shifts as a function of pressure. This parameter examines the nature of pure quasiharmonicity in a material because

it accounts for frequency shifts only due to changing volume (because decreasing the ambient pressure increases the volume of a material). The isobaric Gruneisen parameter probes both the effects of quasiharmonicity and anharmonicity by elucidating the effect of both temperature and temperature dependent volume on the frequency shifts. From fig. 3.19 we calculate the isobaric Gruneisen parameter for each of the 5 phonon modes. We also calculate the averaged isobaric Gruneisen parameter from eq. 3.23. These values are listed in table 3.1.

	Experimental	Approximately QHA
γ: Low Transverse Acoustic	5.75	1-2
γ: High Transverse Acoustic	5.16	1-2
γ: Longitudinal Acoustic	5.04	1-2
γ: Low Transverse Optical	1.61	1-2
γ: Longitudinal Optical	4.01	1-2
γ: Thermal Average	4.31	1-2

Table 3.1: Table of experimentally determined Gruneisen parameter and the associated expected Gruneisen parameter in the QHA

We also compare these values to values for the Gruneisen parameter that we would expect in the quasiharmonic approximation. It is often stated that the mode Gruneisen parameter should be between 1 - 2 in the quasiharmonic approximation [9]. It is immediately evident that the Gruneisen parameter parameter is much higher than that predicted by the QHA for all the modes except the low-energy transverse optical mode. The thermally average Gruneisten parameter is also much higher at about a factor of 4 larger than expected. Further analysis of these Gruneisten parameters is left for the discussion section.

From eq. 2.29 recall that, to first order, the phonon DOS is the only function needed to calculate the vibrational entropy. We calculate the vibrational entropy in 2 methods. We first assume a purely harmonic approximation. In this regime, the phonon DOS should not vary

with temperature. We substitute the phonon DOS at 296 K into eq. 2.29 and numerically calculate the integral. We use this same DOS for all higher temperatures and rely on the temperature dependence of the Planck distribution to yield a temperature dependent vibrational entropy. The result of doing so is plotted below in fig. 3.20.

We have overlaid the vibrational entropy calculated in the harmonic approximation with the total entropy. The total entropy is from the Scientific Group Thermodata Europe (SGTE) database [10]. The data is in the form of the Gibbs free energy and is differentiated to yield the total entropy. We observe that the harmonic approximation shows that the vibrational entropy accounts for most of the total entropy at low temperatures, but shows that the vibrational entropy makes up less and less of the total entropy at higher temperatures. We go a step further and use the true phonon DOS calculated at each temperature. We then perform the same numerical integral to yield the plot below (fig. 3.21).

The similarity between the vibrational entropy and the total entropy is striking. The vibrational entropy makes up almost all of the total entropy at all the temperatures we found phonon DOSs. Note that the vibrational entropy dips slightly below the total entropy at temperatures above 1000 K. Further analysis of the relationship between the total entropy and vibrational entropy, especially at higher temperatures is left for the discussion.

3.8 Discussion

Studies of the phonon DOS at temperatures up to close to the melting point of germanium have allowed us to observe the effects of germanium's anharmonicity. The first observations we made were in the shifts of phonon frequency. From the fig. 3.17 it is evident that all

the phonon modes experience thermal softening. Is this softening enough to be characterized by quasiharmonic theory alone? It seems like the answer is no. The isobaric Gruneisen parameter for most materials in the QHA is cited to be between 1 and 2. We also point to a study done by Kim et al. where they do An initio DFT and density functional perturbation theory (DFPT) calculations on silicon to determine a calculated thermally averaged isobaric Gruneisen parameter of 1.102 ± 0.72. Since Si and Ge are so chemically similar because of their relative positions on the periodic table, we expect their computationally calculated Gruneisen parameters in the QHA to be at least somewhat alike. We calculate a thermally averaged isobaric Gruneisen parameter of 4.31, which is a factor of 2 - 4 larger than that we would expect from QHA theory alone. It is noteworthy that the low-energy transverse optical mode adheres to the predicted Gruneisen parameter value. It could indeed be that this mode is well described by QHA, while the other modes are not.

The failure of QHA to account for all the thermal softening stems from the assumption that phonons are noninteracting. In reality, expanding the potential between atoms out to higher orders reveals multi-phonon processes, often enabled by cubic and quartic terms in the hamiltonian. These phonon-phonon interactions can serve to exacerbate thermal softening in some materials. Evidently Ge is one of those materials.

We also examined the vibrational contribution to the total entropy in Ge. When we used only the phonon DOS from 296 K, we found values for the vibrational that were far from the total entropy, as expected. The inability to account for all the entropy of vibration is one of the flaws of the naive harmonic model. We then calculated the vibrational entropy contribution by using the true phonon DOS we calculated earlier in this chapter. The vibrational entropy was able to account for almost all the total entropy at every temperature,

with an agreement to within 1%. This is especially noteworthy because the total entropy was calculated by calorimetry-like measurements, while our calculations were done by counting phonons! It has been known for quite some time that phonons make up most of the entropy of materials at at least low and moderate temperatures . We find that this statement is indeed still valid at higher temperatures. We also note, however, that there is a small difference between the vibrational entropy and total entropy at temperatures above 1000 K. This may suggest a small additional contribution to the total entropy at higher temperatures.

3.9 Future Work

Before submitting for possible publication we would like to computationally calculate both a mean Gruneisen parameter and a mean isobaric Gruneisen parameter in the QHA. This would allow us to quantitatively compare the Gruneisen parameters we calculated through experiment with those calculated through computation in the QHA. As stated before, it would be surprising if these values were computed to be well above 2.

To perform the calculation we would perform ab initio DFT and DFPT calculations performed with the VASP package. A plane-wave basis set and Perdew-Burke-Ernzerhof (PBE) exchange correlation functionals [11] for projector-augmented-wave pseudopotentials [12] could be used with the generalized gradient method. We could minimize the free energy with respect to the supercell volume to obtain QHA calculations. Ground state energies could finally be calculated for each volume, and the DOS would be calculated with the lattice parameter that minimized the volume. With these temperature dependent DOS in hand, the rest of the analysis would follow as above.

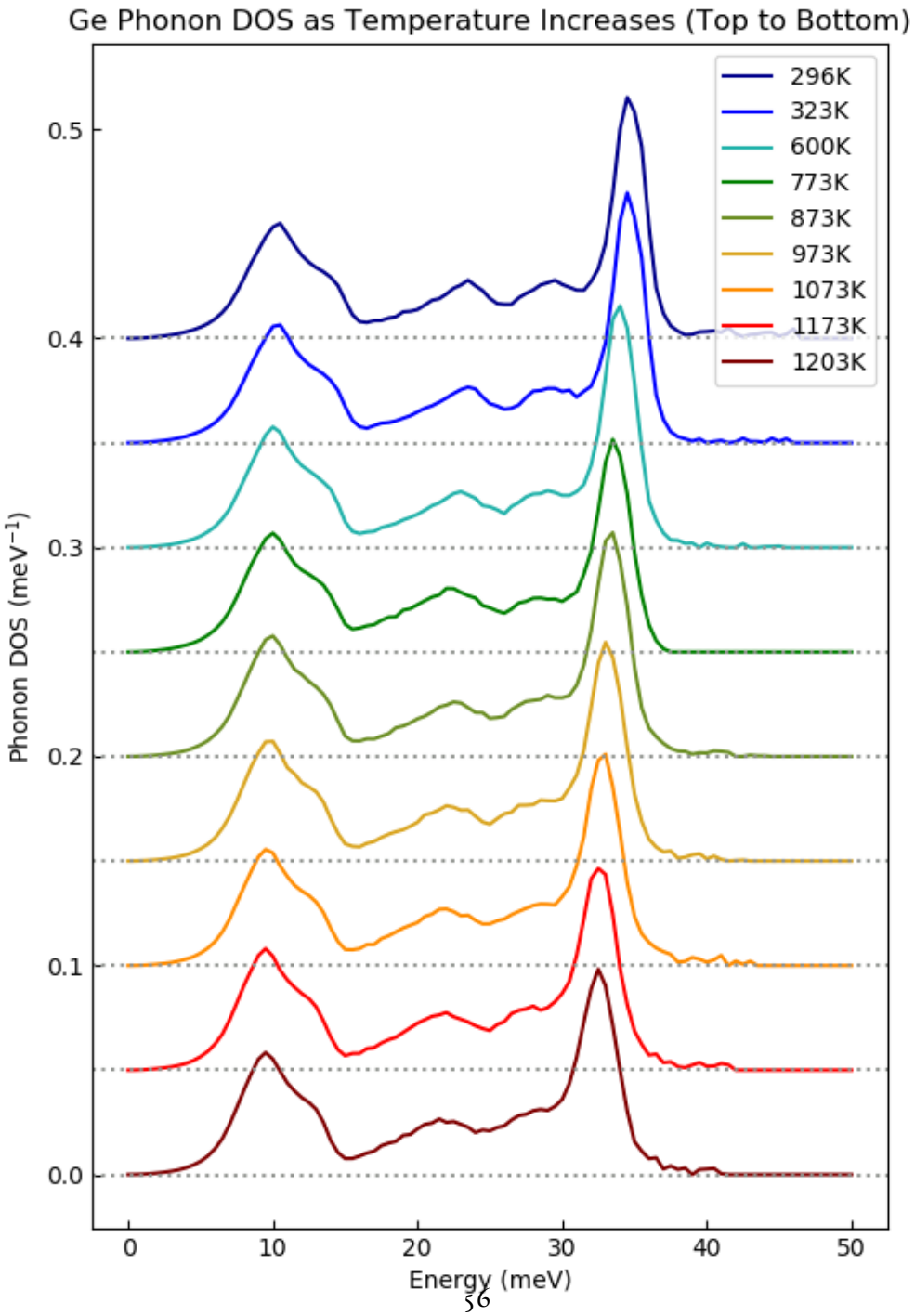

Figure 3.17: Phonon DOS curves of Ge normalized to unity. Curves are offset on the energy-axis for clarity

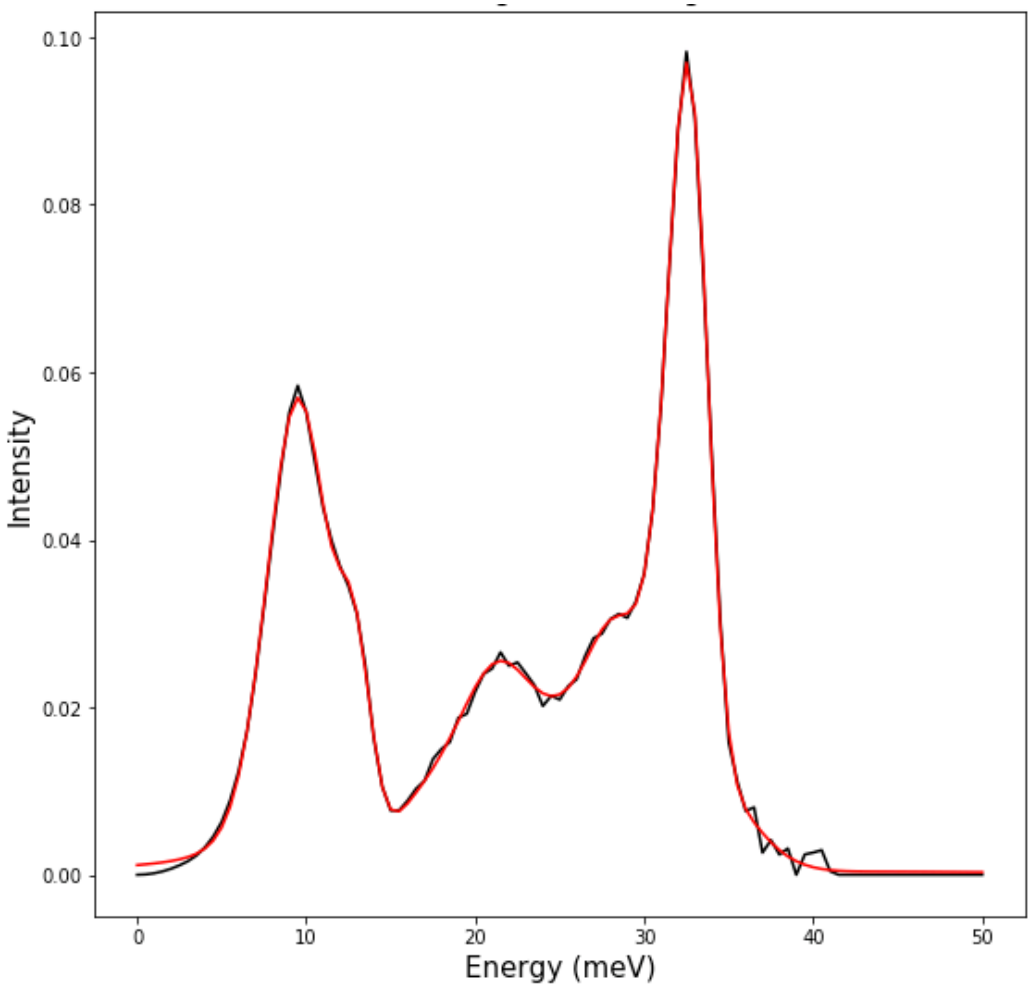

Figure 3.18: 1203 K phonon DOS with the 5 fitted Gaussians overlayed.

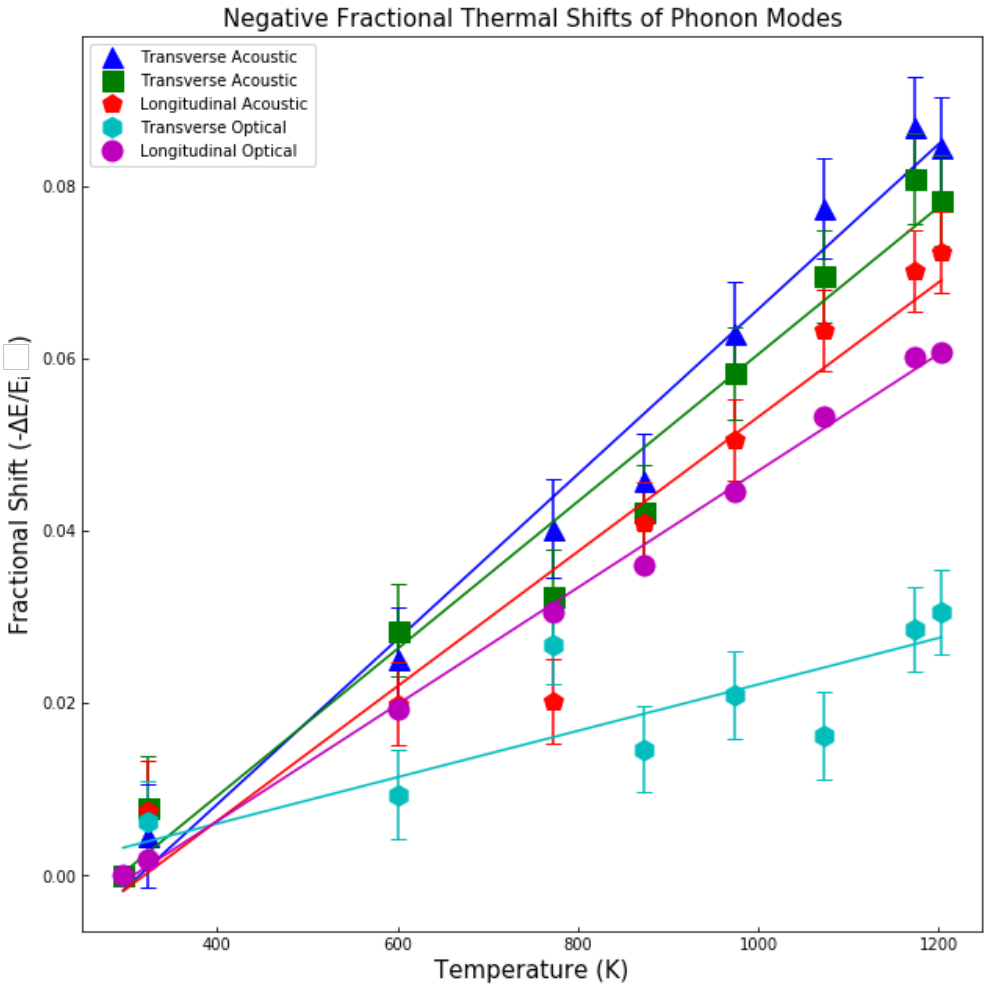

Figure 3.19: Negative fractional thermal shifts of phonon modes. The y axis is the fractional shift, so, for example, a value of 0.06 means a 6% fractional shift

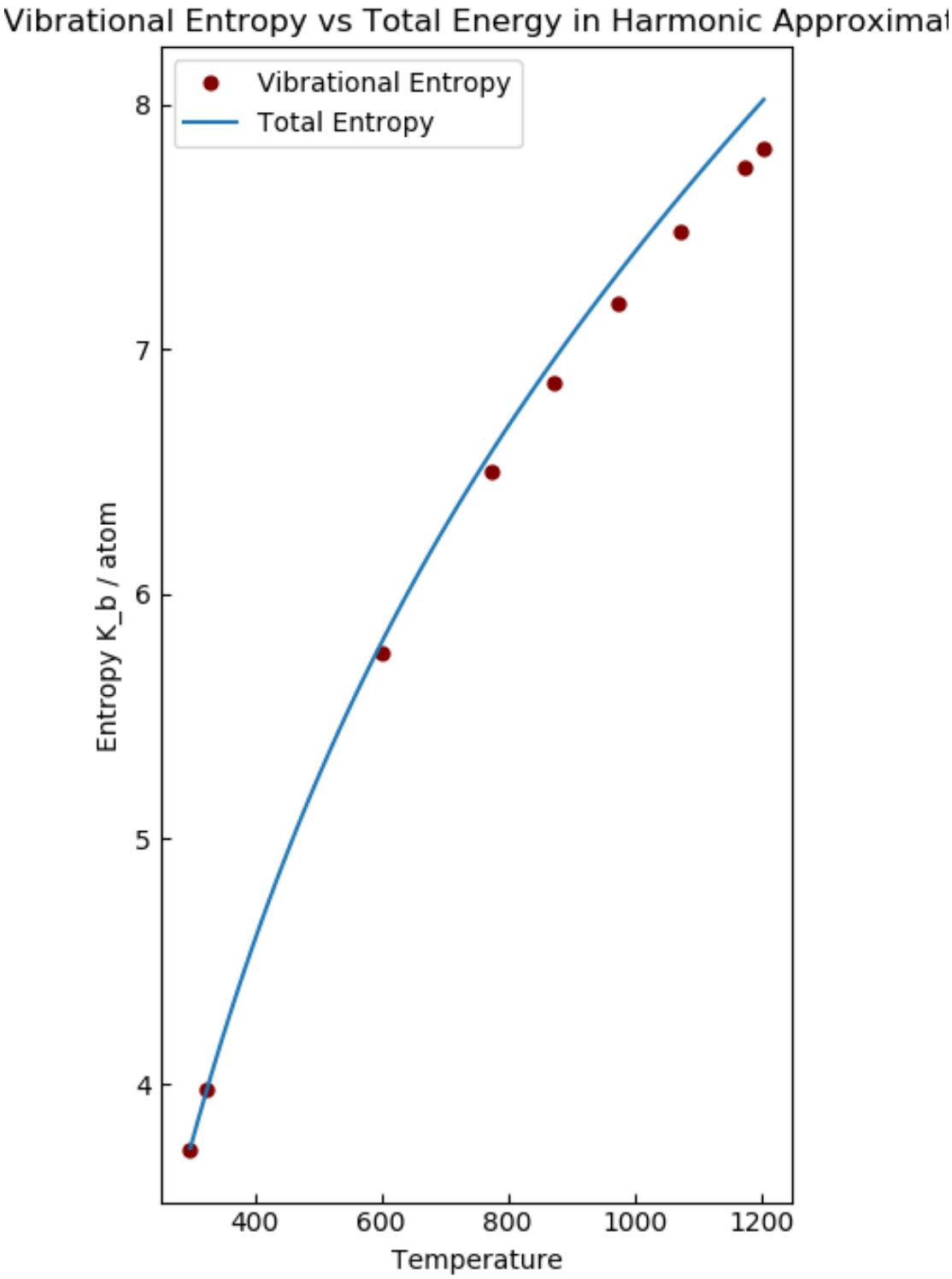

Figure 3.20: Vibrational Entropy vs Total Entropy assuming a purely harmonic approximation

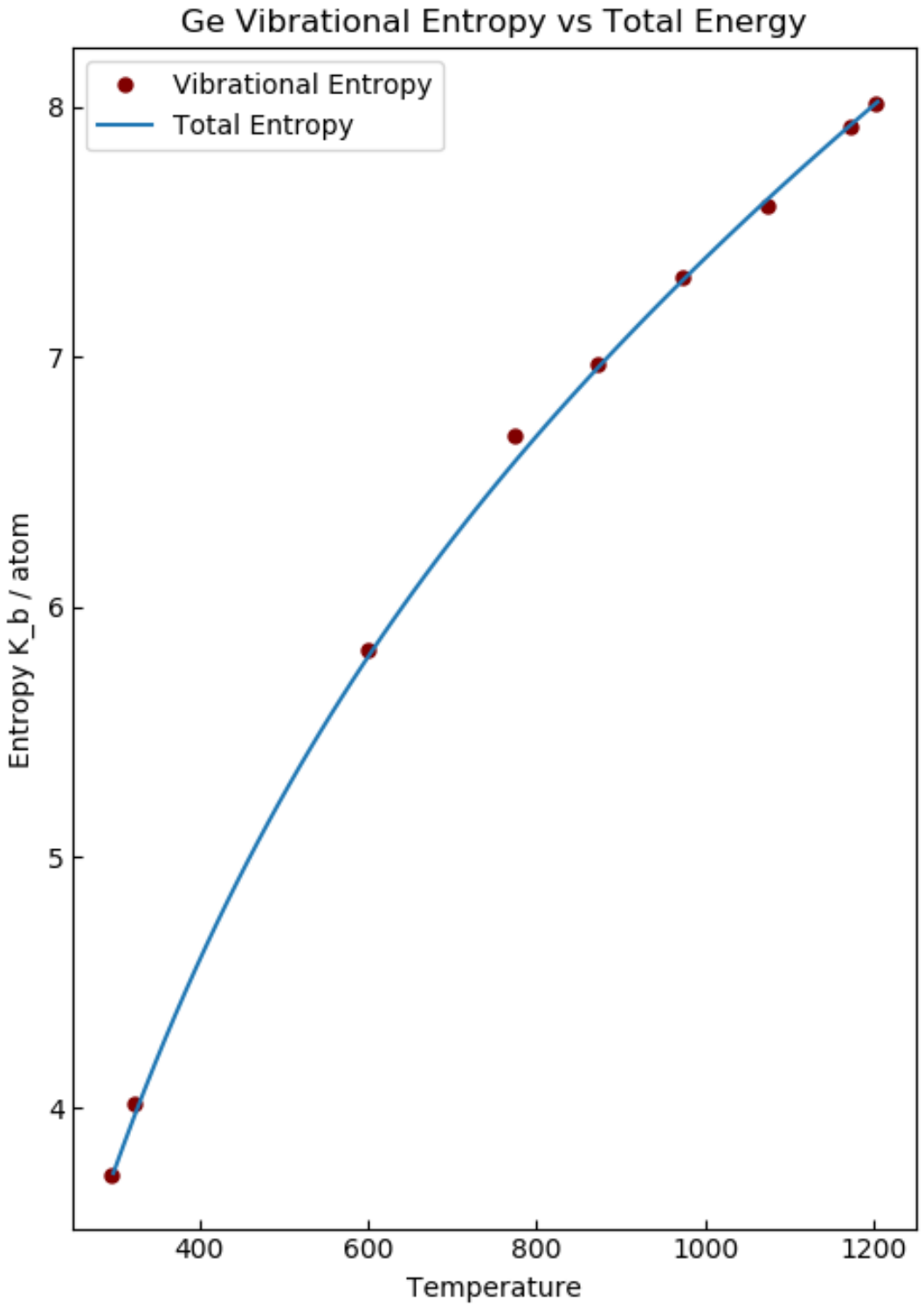

Figure 3.21: Vibrational Entropy vs Total Entropy using the true, experimental phonon DOS

The neutron gods have failed us.

Camille Bernal and Shiva Mudide

4

Liquid Analysis

4.1 Melting at Caltech

The work on the liquid analysis was largely postponed for this thesis due to delays at ARCS. The main experiment which was intended was pushed to sometime in the next year. Much work was still done in preparing for this intended experiment, however. A large portion of the

Fall term was spent testing containment of Sn, Bi, and Pb under melting in quartz ampuoles. Glassblowing and vaccume sealing had to be learned in order to create the quartz ampuoles. Below is an image of the glassblowing torch that was used.

We have also included an image of some example samples of Sn, Bi, and Pb that were melting. All samples were labeled with their respective elements and masses. About 20 samples were melted in all.

Several experimental problems were overcome while melting the metals in the fall term. For example, some of the quartz ampules proved to be too thin for the vacuum pipes. Tubes that allowed for intake of the quartz ampules while allowing for entry to the vacuum had to be procured in order to create a multi-pipe system (fig. 4.3).

4.2 Future Work and Bayesian Analysis

Calorimetry has been used for many years to measure the latent heat of melting, L, yielding the difference of the solid and liquid entropies. Richard's Rule states that the entropy of melting is around 1 k_B per atom. In reality, the entropy of melting can from about 0.5 to nearly k_B per atom. We wish to better understand the contributions to the entropy of melting so that we can test various theories about the underlying physics of melting.

We have proposed to determine the phonon Density of states for Sn, Bi, and Pb as they are heated through their melting temperatures. We would then use eq. 2.29 to calculate the vibrational contribution of entropy to the total entropy. This would allow us to better understand the various theories behind the physics of melting, such a the vibration-transit theory of D.C Wallace coworkers .

4.2.1 Bayesian Analysis

It may also be useful to determine how many phonon modes there is the most evidence for in the liquid state. There is usually the most evidence for 5 or 6 phonon modes in materials with two atoms per unit cell. These modes may collapse in the liquid phase and it is not always clear how many it makes the most sense to try to resolve.

We therefore developed a method for determining the number of peaks that there is the most Bayesian evidence in a Q-cut of the S(Q, E). We have tested the validly of our method on simulated data.

We write E in terms of ω here. Mathematically we can describe a Q-cut of $S(\vec{Q}, \omega)$ as the sum of lorentzians and a single delta function [13]. The lorentzians model the quasielastic and inelastic peaks, while the delta function models the elastic peak. At a given momentum transfer, $\vec{Q}$, we have,

$$S(\omega) = \left[A_0 \delta(\omega) + \sum_{i=1}^{M} A_i \frac{y_i}{\pi(\omega^2 + y_i^2)} \right] * R(\omega) + B(\omega) \tag{4.1}$$

ω is proportional to the energy transfer by $E = \hbar\omega$, R is the instrument resolution function, and B is the background signal. The background signal is present because when we have a sample we have to place it in a quartz container so it does not damage the experimental apparatus at ARCS. The delta function has an amplitude and each lorentzians has its own width and amplitude. We wish to use Bayesian methods to fit for these 2M + 1 parameters, where M is the number of inelastic peaks.

We will also model them as damped harmonic oscillators.

Another question, however, is the number of peaks themselves. Our formulation allows

M to vary from 0 to infinity. We wish to also use Bayesian methods to do model selection, in that we will select for the number, M, inelastic peaks which best fits the data. Our methods will be therefore divided into two sections. Parameter estimation and model selection.

4.2.2 Parameter Estimation

The data from ARCS will, as we have seen, be a blurred and noisy version of the true spectrum. We have taken this into account with the noise term, in addition to the background term from the empty chamber scattering. We assume that the shape of the resolution function does not vary with position in the convolution.

Parameters estimation comes into play assuming we have already done model selection; however, we describe the methods of parameter estimation first because they are simpler and foundational. Once we have done model selection we will have a best estimate as to the number of inelastic peaks, M, in our data. Our job now is to estimate the 2M+1 unknown parameters of interest. Formally, we would like to calculate the 2M + 1 dimensional probability density function (PDF) for the parameters given the data and M. We denote the PDF of some random variable, X as $P(X)$.

The PDF for the parameters given the data and the number of peaks M is then

$$P(A_0, \{A_i, y_i\}|M, \{D_k\}) \tag{4.2}$$

We call this PDF the posterior PDF because it represents our beliefs about the probability densities of the parameters values after we have analysed the data. This in contrast to our prior beliefs which are represented by a prior PDf.

If we have this function in hand, we can find its maximum to give our best estimate of the

parameters. We can also calculate the reliability of our parameters by the width of the posterior about its highest peak. This function seems impossible to calculate at first glance. How are we supposed to calculate the probability of our different hypotheses for the parameters given the data? We must recast the problem into one that is represented by a conditional probability that we can indeed compute. That's where Bayes' theorem comes in.

We use Bayes theorem to relate the posterior to our prior beliefs about the parameters and the likelihood that we would observe the data given each of our hypotheses. Formally we have,

$$P(A_0, \{A_i, y_i\}|M, \{D_k\}) \propto P(A_0, \{A_i, y_i\}|M) \times P(\{D_k\}|A_0, \{A_i, y_i\}, M) \tag{4.3}$$

The likelihood measures the relative likelihood that we would obtain our data for each point in parameter space. Multiplying it by the prior updates our beliefs about the underlying PDF after viewing the data.

We assume the greatest amount of ignorance about our parameter values by setting the prior constant,

$$P(A_0, \{A_i, y_i\}|M) = constant \tag{4.4}$$

The posterior is then proportional to the likelihood. All that is left to do is calculate this likelihood function.

Instead of maximizing the likelihood we minimize the negative of the log of the likelihood.

Let $\vec{X} = \{A_0, \{A_i, y_i\}\}$ to reduce clutter.

$$P(\{D_k\}|\vec{X}, M)$$

$$= P(\{S_k\}, \{\omega_k\}, \{\sigma_k\}|\vec{X}, M) \tag{4.5}$$

$$= P(\{\omega_k\}) \times P(\{\sigma_k\}|\{\omega_k\}) \times P(\{S_k\}|\{\omega_k\}, \{\sigma_k\}, \vec{X}, M) \tag{4.6}$$

$$= \prod_{k=1}^{N} P(\omega_k) \times P(\sigma_k\,|\omega_k) \times P(S_k|\omega_k, \sigma_k, \vec{X}, M) \tag{4.7}$$

$$= \prod_{k=1}^{N} P(\omega_k) \times P(\sigma_k\,|\omega_k) \times \frac{1}{\sqrt{2\pi}} \exp\left\{-\frac{1}{2}\left(\frac{S_k - \mu_k}{\sigma_k}\right)^2\right\} \tag{4.8}$$

Taking the negative natural log yields,

$$-log(P(\{D_k\}|\vec{X}, M))$$

$$= \sum_{k=1}^{N}\left[-logP(\omega_k) - logP(\sigma_k|\omega_k) - log\left(\frac{1}{\sqrt{2\pi}}\right) + \frac{1}{2}\left(\frac{S_k - \mu_k}{\sigma_k}\right)^2\right] \tag{4.9}$$

$$= constant + \sum_{k=1}^{N} \frac{1}{2}\left(\frac{S_k - \mu_k}{\sigma_k}\right)^2 \tag{4.10}$$

We therefore minimize,

$$\sum_{k=1}^{N} \frac{1}{2} \left(\frac{S_k - \mu_k}{\sigma_k} \right)^2 \tag{4.11}$$

where,

$$\mu_k = \left[A_0 \delta(\omega_k) + \sum_{i=1}^{M} A_i \frac{y_i}{\pi(\omega_k^2 + y_i^2)} \right] * R(\omega_k) + B(\omega_k) \tag{4.12}$$

to find our optimal estimation of the parameters.

We have assumed, in the above derivation, that each data point is independent and subject to additive Gaussian noise (another way of thinking about this is that each datum is drawn from its own Gaussian process).

Note that the likelihood is a function of $\vec{X}$, which has dimensionality 2M + 1. We need to discretize this space and calculate the value of the likelihood at each point in this space. The calculation of the likelihood at each point is of order N. This "grid-search" method is unnecessarily computationally expensive. A common method of constructing the posterior is using a Markov Chain Monte Carlo (MCMC) algorithm. We instead opt to use yet another approach, which will be described in the algorithm section.

4.2.3 Model Selection

The derivations for parameter estimation above assumed that we knew the number, M, of inelastic peaks. How can we calculate what is the most likely value for M? We need to find the posterior probability density function for M. Using Bayes' theorem like above yields,

$$P(M|\{D_k\}) \propto P(M) \times P(\{D_k\}|M) \tag{4.13}$$

for the probability of having M lorentzians given the observed data.

We have no reason to assume that the number of peaks is larger than a few (between 5 and 15). We could increase the upper bound if needed, if we notice that the posterior is increasing as we increase M. We again assume maximum ignorance and assign a uniform prior on the number of peaks. The posterior is then proportional to the likelihood of observing the data given a choice for M. To find the likelihood, we need to integrate over all possible ways that we could observe the data given some fixed M. This is a marginal integral, as a function of M, over the parameter space. Namely,

$$P(\{D_k\}|M) = \int \cdots \int P(\{D_k\}, A_0, \{A_i, y_i\}|M)\, dA_0 d^M A_i d^M y_i \tag{4.14}$$

The integrand is just the product of the prior and likelihood function for the parameters,

$$P(\{D_k\}, A_0, \{A_i, y_i\}|M) = P(A_0, \{A_i, y_i\}|M) \times P(\{D_k\}|A_0, \{A_i, y_i\}, M) \tag{4.15}$$

This is is the normalization factor we ignored previously! We refer to it as the evidence, because it gives us information about the amount of evidence for the data given a specific value for M. We take uniform priors for our width and amplitude parameters. We set the y_{max} to be the energy range of the data and A_{max} to be the total integrated intensity of the data. y_{min} and A_{min} are both zero. We could use MCMC directly on the multidimensional integral to yield a representation of the posterior distribution of M. To avoid computing a 2M + 1 dimensional integral with an integrand of the sum of N terms, we can instead make a further simplification analytically. Taylor expanding about the maximum allows us to relate the equation to a 2M + 1 dimensional multivariate Gaussian and exponential of the posterior

for a given M. Permuting the indices associated with the peak intensities and solving for the posterior yields (see [14] for more details),

$$P(M|\{D_k\}) \propto \frac{M!(4\pi)^M}{(y_{max}A_{max})^M\sqrt{det\left(\nabla\nabla\left[\sum_{k=1}^{N}\left(\frac{S_k-\mu_k}{\sigma_k}\right)^2\right]\right)}} \times \exp\left(-\frac{1}{2}\left[\sum_{k=1}^{N}\left(\frac{S_k-\mu_k}{\sigma_k}\right)^2\right]_{min}\right) \tag{4.16}$$

$\left[\sum_{k=1}^{N}\left(\frac{S_k-\mu_k}{\sigma_k}\right)^2\right]_{min}$ is the best fit value assuming M lorentzians. The term inside the determinant is the hessian matrix evaluated at that best fit value. This looks monstrous but it is not terribly unintuitive. The exponential is proportional to the best-fit likelihood. The other terms are the multivariate equivalent of the Ockham factor, namely the ratio of the 2M + 1 dimensional hypervolumes allowed by the posterior, in the parameter space $\{A_i, y_i\}$.

4.2.4 Algorithm

MCMC was initially used to calculate the posterior. This proved to be computationally intensive even while using the emcee python package. We instead adopt an algorithm described in Sivia chapter 4 [14]based on discrete 1-dimensional searches and linearised multidimensional optimization. We study the algorithm presented in Sivia in detail and implement it using Scipy's Newton-Raphson routine [15]. We describe the main ideas below.

We take the background to be linear and parameterized by two nuisance variables. We then add another nuisance parameter for any possible energy offset in the experimental apparatus. We use the Newton-Raphson algorithm to refine the nuisance parameters described above and the amplitude of the elastic scattering delta function. The Newton-Raphson algorithm

yields $\left[\sum_{k=1}^{N}\left(\frac{S_k-\mu_k}{\sigma_k}\right)^2\right]_{min}$ and the determinant of the hessian matrix by computing first and second derivatives of $\left[\sum_{k=1}^{N}\left(\frac{S_k-\mu_k}{\sigma_k}\right)^2\right]$ with respect to the above parameters. We then calculate the posterior probability for there being no inelastic peaks (M = 0).

Next we search for the optimal width of a potential lorentzian component with a linear search. We then keep the energy offset parameter fixed, yielding a simple linear problem for the optimization of A_0 and A_1 at a given width. We next refine all our parameters in the M = 1 model with Newton-Raphson. We can finally then invoke eq. 4.16 again to calculate the posterior probability for there being one inelastic peaks (M = 1).

We continue like this, again and again, adding one more peak at a time until a maximum in the posterior PDF for M is clear. We, of course, abide by Ockham's razor and stop adding peaks when it becomes evident that we can achieve a good fit with a small number of peaks.

4.2.5 Results

We test our methods and code by using them to analyze simulated data.

4.2.6 Simulated Data

We simulate data from the model described in eq. 4.1. We choose a standard resolution function to convolve with. We add gaussian noise to each measurement. We then answer, how many inelastic peaks is there the most evidence for in the data? We also find estimates for the amplitude and width of the peaks, as well as our estimates' uncertainties. These are found using the algorithm described in section (3). We did not explicitly mention it in section (3), but the uncertainties are found from the diagonal components of the inverse of the hessian,

as is standard to achieve the correct marginal error bars.

We generate data from the sum of one inelastic peak with width $100\mu eV$ and one elastic peak. We give the elastic peak a relative amplitude of 5 and the inelastic peak a relative amplitude of 15.*

Running our code yields the following posterior distribution for the number of inelastic peaks, M,

The maximum a posteriori estimate for the number of peaks is 1. This is a factor of around 1000 greater than the posterior for 0 peaks and is at least 10 times greater than values of $M \geq 2$. The Newton-Raphson routine described above yields us $\left[\sum_{k=1}^{N}\left(\frac{S_k-\mu_k}{\sigma_k}\right)^2\right]_{min}$ and the hessian, but not the entire posterior. At the benefit of computational feasibility we lose the descriptive joint PDF corner plots that MCMC gives us. Nevertheless, we can still report our best estimates of the amplitudes and widths of the peaks, as well as our uncertainties.

We estimate the relative amplitudes of the peaks to be 4.93 ± 0.18 and 15.32 ± 0.54 for the elastic and inelastic peaks, respectively. We estimate the width of the inelastic peak to be $98.2 \pm 3.5\ \mu eV$.

These are within 4% of the true values that we used to generate the data. Our posterior for M also makes sense.

We see a sharp decline to the left of M = 1 because there is not enough structure in having no inelastic peaks to support the data. We see a slower decline to the right of M = 1 because the model is becoming unnecessarily more complicated. Here we effectively capture Ockham's razor. Our best estimate for the number M is the value that is the lowest and is still consistent with our data.

*I debated on whether to inform the reader how I generated the data before or after I show plots of my results. I suppose this is a bit like telling the punchline of a joke, but sometimes it's better that way.

Figure 4.1: An image of the glassblowing torch used to seal the quartz ampules.

Figure 4.2: An image of some of the melted samples demonstrating containment.

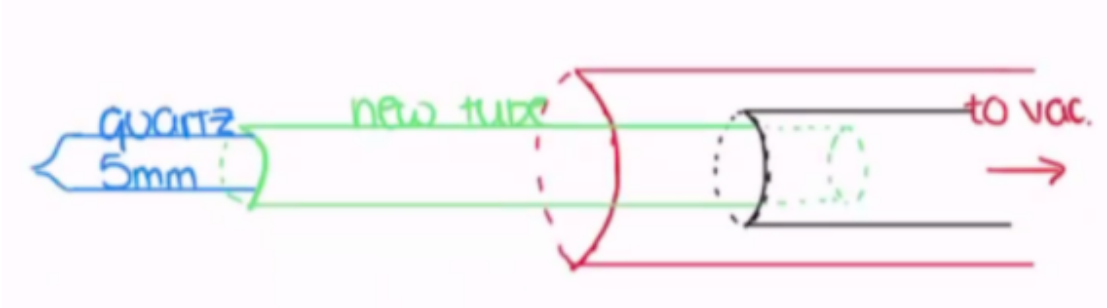

Figure 4.3: Image credit: Camille Bernal. The multi-tube system used to accommodate for some the thinner quartz ampules.

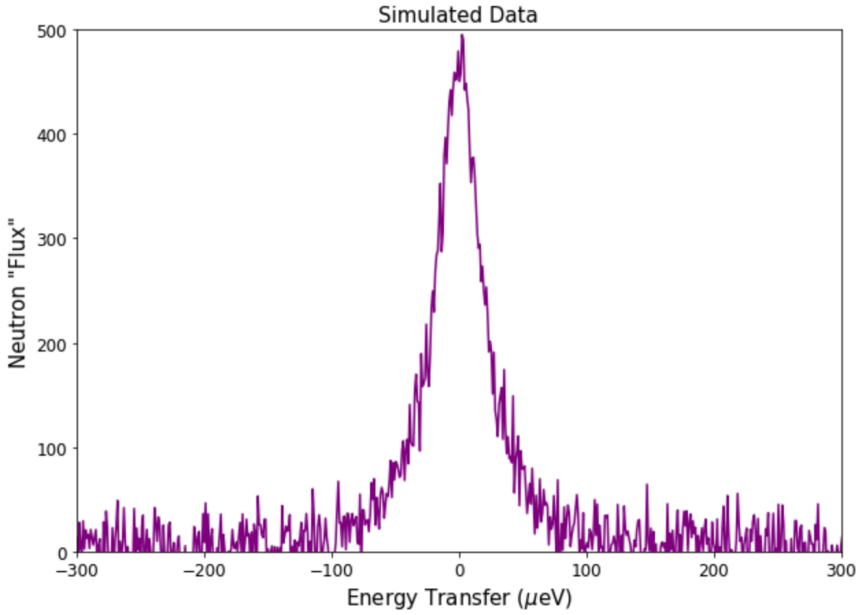

Figure 4.4: The Simulated Data

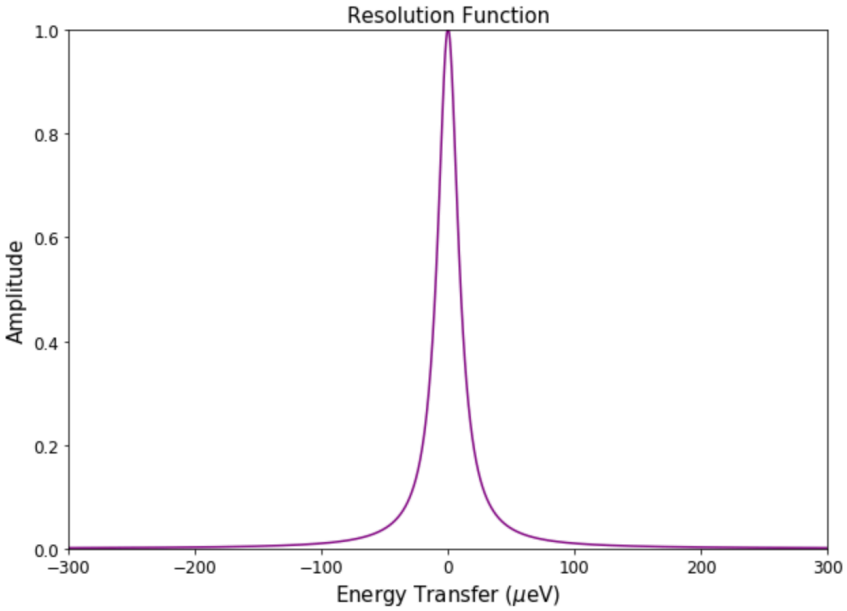

Figure 4.5: Our Resolution Function

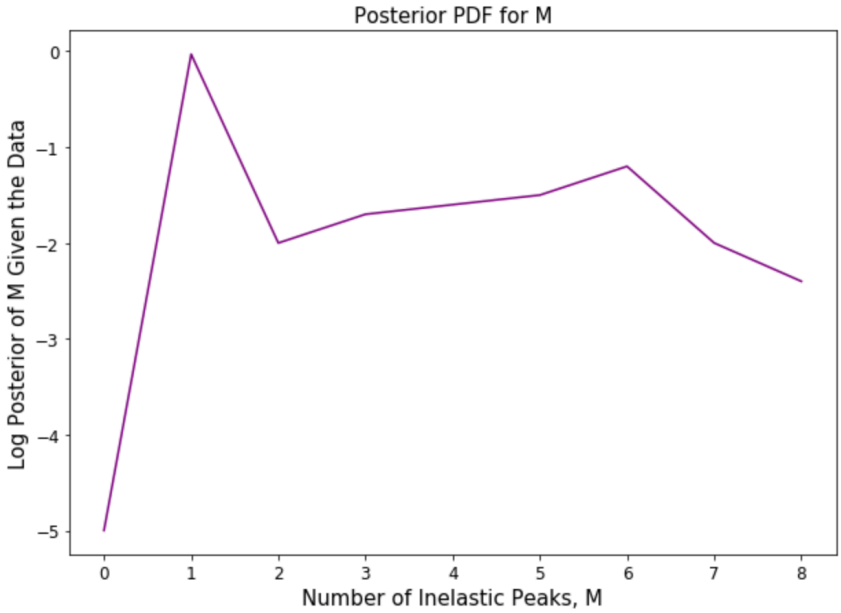

Figure 4.6: Posterior Probability for the Number of Inelastic Components

References

[1] Proline Server. Two-dimensional bravais lattices. *CC BY-SA 3.0*, 2018.

[2] Max Kresch. Temperature dependence of phonons in elemental cubic metals studied by inelastic scattering of neutrons and x-rays. *Caltech Thesis*, 2008.

[3] Brent Fultz. Phase transitions in materials. *Cambridge University Press*, 2020.

[4] Léon Van Hove. Correlations in space and time and born approximation scattering in systems of interacting particles. *Physical Review 95.1*, page 249, 1954.

[5] Fahima Islam Lin, Y. Y. and Max Kresh. Vibrational thermodynamics of materials. *Progress in Materials Science*, pages 247–352, 2010.

[6] Philip Phillips. Advanced solid state physics. *Cambridge University Press*, 2012.

[7] Dennis Kim. Phonon anharmonicity in silicon from 100 to 1500 k. *Physical Review B*, 2015.

[8] Fahima Islam Lin, Y. Y. and Max Kresh. Multiphonon: Phonon density of states tools for inelastic neutron scattering powder data. *Journal of Open Source Software*, 2018.

[9] Pavel A. Korzhavyi and Jing Zhang. Free energy of metals from quasi-harmonic models of thermal disorder. *Metals*, 2021.

[10] Alan Dinsdale. Sgte data for pure elements. *Calphad*, pages 317–425, 1991.

[11] Kieron Burke Perdew, John P. and Matthias Ernzerhof. Generalized gradient approximation made simple. *Physical review letters*, 1996.

[12] Georg Kresse and Daniel Joubert. From ultrasoft pseudopotentials to the projector augmented-wave method. *Physical review b*, 1999.

[13] Fanni Juranyi Jan Peter and Rolf Hempelmann. Introduction to quasielastic neutron scattering. *Zeitschrift für Physikalische Chemie*, pages 5–32, 2010.

[14] Devinderjit Sivia and John Skilling. Data analysis: a bayesian tutorial. *OUP Oxford*, 2006.

[15] Pauli Virtanen et al. Scipy 1.0: fundamental algorithms for scientific computing in python. *Nature methods*, pages 261 – 272, 2020.